

# Thesis Title

by

E. Ross



A thesis submitted to the  
University of Birmingham  
for the degree of  
DOCTOR OF PHILOSOPHY

Solar and Stellar Physics Group (SASP)

School of Physics and Astronomy

University of Birmingham

Birmingham, B15 2TT

Month 20XX

# Contents

<b>List of Figures</b>	<b>vi</b>
<b>List of Tables</b>	<b>vii</b>
<b>List of Abbreviations</b>	<b>ix</b>
<b>1 A Frequency Domain Investigation on the Morphology of the Solar Mean Magnetic Field</b>	<b>1</b>
1.1 Introduction . . . . .	1
1.2 Aims . . . . .	5
1.3 Data . . . . .	6
1.3.1 Summary of the Data Set . . . . .	6
1.3.2 Obtaining the SMMF from BiSON . . . . .	7
1.3.3 Comparison between WSO and BiSON . . . . .	10
1.4 Methodology . . . . .	14
1.4.1 Identifying Features in the SMMF Power Spectrum . . . . .	14
1.4.2 Parameterisation of the SMMF Power Spectrum . . . . .	16
1.4.3 Comparison with the WSO SMMF . . . . .	19
1.5 Results . . . . .	19
1.5.1 Investigation of the Window Function . . . . .	19
1.5.2 Modelling the BiSON Power Spectrum . . . . .	25
1.5.3 Comparison to the WSO Power Spectrum . . . . .	29
1.6 Discussion . . . . .	32
1.6.1 Asymmetry in the Power Spectrum . . . . .	32
1.6.2 Testing the Effects of Differential Rotation and Active Region Migration . . . . .	37
1.6.3 Further Morphology of the SMMF using SDO/HMI Data . . . . .	41
1.7 Conclusion . . . . .	43
<b>2 Rossby Modes in the Solar Mean Magnetic Field</b>	<b>47</b>
2.1 Introduction . . . . .	47
2.2 Aims . . . . .	49
2.3 Theory . . . . .	50
2.4 Methodology . . . . .	51
2.4.1 Testing the Residual Spectrum . . . . .	51
2.4.2 Modelling $r$ mode Profiles . . . . .	54
2.5 Results . . . . .	54

2.5.1	Testing the Residual Spectrum . . . . .	54
2.5.2	Modelling $r$ mode Profiles . . . . .	55
2.6	Discussion . . . . .	58
2.6.1	Manifestation of Rossby Waves in the Power Spectrum . . . .	58
2.6.2	Rossby Modes in Other Sources of SMMF Data . . . . .	62
2.7	Conclusion . . . . .	64
<b>A</b>	<b>Simulations of the Artificial SMMF</b>	<b>66</b>
A.1	Model . . . . .	66
A.2	Configuration of the Simulations . . . . .	68
A.3	Outputs . . . . .	71
	<b>Bibliography</b>	<b>74</b>

# List of Figures

1.1	An example of the BiSON ratios data over a 30-minute period. The separation between the two ratios is due to the solar mean magnetic field. Other excursions in the individual ratios are due to the other effects measured by the RSS. . . . .	9
1.2	(a) 40-second cadence observations of the SMMF from the Sutherland BiSON station between 1992 and 2012. The sense of the field was chosen to match the Chaplin et al. (2003) and the WSO observations, where positive is for a field pointing outwards from the Sun. (b) Power spectrum of the SMMF on a 40-second cadence truncated to $10\mu\text{Hz}$ , however, the nyquist frequency is 12.5 mHz. . . . .	11
1.3	Daily averaged SMMF measured by WSO (blue) and by the Sutherland BiSON station (black). . . . .	12
1.4	Comparisons between the BiSON SMMF data and the WSO SMMF data. (a) The correlation between daily averaged BiSON SMMF and the WSO SMMF. The solid-green line provides the fit to the data, while the dashed-red line shows a 1:1 relation for comparison. (b) Shows a comparison between the power spectra of BiSON and WSO measurements of the SMMF. . . . .	12
1.5	Formation heights of emission lines over the wavelength range used for WSO observations (top) and for BiSON observations (bottom). The vertical lines show the wavelengths of the emission lines used for observations in air (dashed) and in vacuum (solid). This plot was provided in private communication courtesy of Rinat Tagirov using the NESSY code. . . . .	14
1.6	Full power spectrum of the BiSON SMMF on a logarithmic scale up to the Nyquist frequency. . . . .	15
1.7	Locations of aliased power in side-band peaks. The orange, dotted-lines show the locations of frequencies at multiples of 1/day. The green, dashed-lines show the locations of the side-band peaks – harmonic frequencies reflected around multiples of 1/day. The inset shows a zoom of one set of side-band peaks around 1/day. . . . .	20
1.8	(a) The effect on the power spectrum due to periodic gaps in the data. (b) The effect of the convolution between the window function and the input power spectrum used to make the fake data, highlighting the need to correctly adjust the power for the duty cycle. . . . .	22

1.9	Full, modelled power spectrum of the BiSON SMMF on logarithmic axes. The data are displayed in black and the convolved model using asymmetric Lorentzian peaks is shown in green. . . . .	28
1.10	Full, modelled power spectrum of the WSO SMMF on logarithmic axes. The data are displayed in black and the convolved model using asymmetric Lorentzian peaks is shown in blue. . . . .	31
1.11	(a) Shows the KDE of the monthly averaged sunspot number used to draw samples of source seed times; (b) distribution of the rotation frequency of sources sampled from the KDE, after using the model for the migration and differential rotation. . . . .	33
1.12	(a) Shows the latitudinal migration model as a function of time for each model; (b)-(d) shows the distribution of the rotation frequencies of sources sampled from the KDE for linear, quadratic, and exponential migration models, respectively. . . . .	34
1.13	The median value of the fitted global asymmetry parameter for several simulations of artificial data. The colour represents the migration model used: linear:blue; quadratic:orange; exponential: green. The marker represents the source model used: cosine:circle; sign change:cross; combinations of the cosine and sign change models in ratios of 5:95:downwards triangle; 10:90:plus; 20:80:upwards triangle. . . . .	35
1.14	(a) Shows the Lorentzian distribution peak before and after the time-averaged broadening, and the fit to the broadened peak. (b) Shows the peak distribution before and after the analytical broadening, and the fit to the broadened peak. In both plots the broadened peaks have been shifted by the relevant frequency to overlay them on top of the true $\nu_0$ for comparison. . . . .	40
1.15	Investigations of timescales in the SDO/HMI magnetograms over 2011 and 2014. Both plots show in the top panel, the hemispheric Mean Magnetic Field (MMF) and full-disk Solar Mean Magnetic Field (SMMF) from the magnetograms. The lower panel of each plot displays a comparison between the hemispheric and full-disk mean of the synoptic charts, compared to the box-car smoothed MMF from the magnetograms. N: Northern hemisphere; S: Southern hemisphere. Full HMI: considers the full solar disk; 99 HMI: considers only the inner 99% of the solar disk, by radius. . . . .	42
2.1	Full, modelled power spectrum of the BiSON SMMF on logarithmic axes. The data is displayed in black and the convolved model using asymmetric Lorentzian peaks is shown in green. . . . .	49
2.2	Residual power spectrum of the BiSON SMMF. Over plotted in the green curve is the model of the main SMMF signal. Also over plotted as vertical solid lines are the expected locations of the 4 lowest-frequency sectoral $r$ modes and the dashed lines, the locations of the $B_0$ variation frequency splitting. Dashed lines represent $\pm 31.7$ nHz (i.e. representing the frequencies of splitting due to the variation in the $B_0$ angle.) . . . . .	55

2.3	Realisations of the statistics tests on the BiSON data for different re-binning factors ( $n$ ). The panels of each sub figure are: (top) the full PSD and fit, (second panel) the full and re-binned residuals, (third panel) the probability of statistical noise in each bin, (bottom) distribution of the residuals compared to a $\chi^2$ 2n-DOF. . . . .	56
2.4	Model fit to the $r$ mode in the BiSON PSD residuals using the median from the parameter posterior distributions. . . . .	57
2.5	Mode displacement schematic for an $l = m = 2$ $r$ mode (Strohmayer & Mahmoodifar, 2014) . . . . .	59
2.6	Time series of the velocity and amplitude modulation toy model simulations. The blue curve shows the velocity modulation, i.e. modulating using a cosine with period of 1 year, whereas the orange curve shows the amplitude modulation, i.e. modulating using a rectified cosine with period 1 year. . . . .	60
2.7	Power spectra for the two modulation methods, showing the difference in the way the modulation has changed the frequency of the observed mode. . . . .	60
2.8	SDO/HMI SMMF split into hemispheres and compared to other SMMF sources during (a) 2011, and (b) 2014. The top panel in each figure shows the north (N), south (S), and total disk-averaged mean magnetic field, for both the full solar disk and from pixels within 99% of solar radius. The bottom panels show a comparison between the SMMF, as observed BiSON, WSO, and SDO/HMI (full disk and the 99% disk). . . . .	61
2.9	Comparison of the power spectra for BiSON, WSO, and SDO/HMI. In both figures, the top panel shows the BiSON PSD and the bottom panel shows either the WSO or HMI PSD. The dashed, black line shows the location of the theoretical $l = 2 = m$ $r$ mode frequency, and the red, solid line shows the location of the peak fit in the BiSON PSD residuals. . . . .	63
A.1	Schematic representations of the two models of the artificial SMMF. (a) shows the cosine model with a single source of constant polarity transiting the visible disk. (b) shown the sign change model whereby there are 2 regions of opposite polarity transiting the disk, and their contribution to the SMMF changes during the transit. . . . .	67
A.2	A single realisation of (a) the cosine model, and (b) the sign change model. . . . .	68
A.3	Flowchart showing the step-by-step processes in the generation of the artificial SMMF time series data. . . . .	69

A.4	(a) the burn-in period required to ensure that the interference of sources stabilises. The dashed-vertical line marks one year, showing the sources have stabilised. (b) histogram of the number of sources which remain in the simulation (out of the 20000 input), after the burn-in is removed. (c) the number of simulated sources on the visible disk over the BiSON observational epoch. (d) the daily-averaged sunspot number (blue, and the monthly-averaged sunspot number (orange)). . . . .	70
A.5	Artificial butterfly diagram generated from the simulations, allowing for the parameters to be drawn from distributions, to add stochasticity into the simulation. . . . .	71
A.6	Limit spectrum from 100 realisations of the cosine model (a) and the sign change model (b) using a single source in each model. . . . .	72
A.7	Time series and power spectra for realisations of the simulations using the cosine and sign change models. . . . .	73

# List of Tables

1.1	Model parameter values for the generation of artificial data, and the median posterior values for the fit to the power spectra generated with and without the gaps in the data. Numbers in brackets denote uncertainties on the last 2 digits, and all uncertainties correspond to the 68% credible intervals either side of the median. . . . .	24
1.2	Median values of the marginalised posterior distributions for each model parameter in the fit to the BiSON power spectrum, adjusted for the duty cycle factor ( $\sim 0.156$ ) in the convolution process. Numbers in brackets denote uncertainties on the last 2 digits, and all uncertainties correspond to the 68% credible intervals either side of the median. . . . .	27
1.3	Median values of the marginalised posterior distributions for each model parameter in the fit to the WSO power spectrum, adjusted for the duty cycle factor ( $\sim 0.778$ ) in the convolution process. Numbers in brackets denote uncertainties on the last 2 digits, and all uncertainties correspond to the 68% credible intervals either side of the median. . . . .	30
1.4	Input line-width and the median posterior values of the Lorentzian model each simulation. Numbers in brackets denote uncertainties on the last 2 digits, and all uncertainties correspond to the 68% credible intervals either side of the median. . . . .	40
2.1	Predicted <sup>+</sup> and observed <sup>o</sup> $r$ mode frequencies for combinations of $l$ and $m$ . Predicted frequencies and conversions of observations to different frames of reference use equation (2.1), equation (2.2), and equation (2.3), with $\Omega = 453.1$ nHz. The predicted splitting for the $B_0$ angle variation is also provided. The key for the source column is: LPT for Löptien et al. (2018), LNG for Liang et al. (2019), and LZA for Lanza et al. (2019). . . . .	51
2.2	Median posterior values of the Lorentzian model for the $r$ mode peak in the BiSON SMMF PSD residuals. Numbers in brackets denote uncertainties on the last 2 digits, and all uncertainties correspond to the 68% credible intervals either side of the median. . . . .	57



# List of Abbreviations

**AR** Active Region.

**BiSON** Birmingham Solar Oscillations Network.

**BMR** Bipolar Magnetic Region.

**EEMD** Empirical Mode Decomposition.

**FA** False Alarm.

**GMF** General Magnetic Field.

**HMC** Hamiltonian Monte Carlo.

**KDE** Kernel Density Estimate.

**LOS** Line Of Sight.

**MCMC** Markov Chain Monte Carlo.

**MFC** Magnetic Flux Concentration.

**MMF** Mean Magnetic Field.

**NLTE** Non-Local Thermal Equilibrium.

**NUTS** No U-Turn Sampler.

**PSD** Power Spectral Density.

**RM** Rotationally Modulated.

**RSS** Resonant Scattering Spectrometer.

**SB** Stochastic Background.

**SDO/AIA** Solar Dynamic Observatory Atmospheric Imaging Assembly.

**SDO/HMI** Solar Dynamic Observatory Helioseismic and Magnetic Imager.

**SMMF** Solar Mean Magnetic Field.

**SOHO/MDI** Solar and Heliospheric Observatory Michelson Doppler Imager.

**SSN** Sun Spot Number.

**WSO** Wilcox Solar Observatory.

# 1 A Frequency Domain Investigation on the Morphology of the Solar Mean Magnetic Field

## 1.1 Introduction

The Sun has a complicated magnetic field structure; many features of the Sun and proxies for the solar activity are related to the evolution of the Sun's magnetic field (Wu et al., 2018).

The Solar Mean Magnetic Field (SMMF) is a surprising, non-zero measurement of the imbalance of opposite magnetic flux polarities observed on the full, visible disk of the Sun (Svalgaard et al., 1975), and is defined as the mean Line Of Sight (LOS) magnetic field when observing the Sun-as-a-star (Scherrer et al., 1977a,b; Garca et al., 1999). In the literature the SMMF is also commonly referred to as the General Magnetic Field (GMF) (Severny, 1971) or the Mean Magnetic Field (MMF) (Kotov, 2008) of the Sun.

Observations of the SMMF have typically been made by measuring the Zeeman splitting of spectral lines using a ground-based Babcock-type magnetograph (Scherrer et al., 1977a), although more recently the SMMF has been calculated from full-disk LOS magnetograms taken from space-borne telescopes such as the Solar Dynamic Observatory Helioseismic and Magnetic Imager (SDO/HMI), in order to

understand the morphology of the SMMF (Kutsenko et al., 2017; Bose & Nagaraju, 2018). It is understood that the strength of the SMMF may vary depending on the spectral line used to measure the SMMF (Kotov, 2008, 2012), however, it is generally accepted in the literature that the SMMF varies slowly with the solar activity cycle, with a amplitude of up to around  $\pm 2$  G during solar maximum and up to around  $\pm 0.2$  G during solar minimum (Plachinda et al., 2011). In addition, the SMMF displays a strong, quasi-coherent rotational signal (Chaplin et al., 2003; Xie et al., 2017), which we assume arises from inhomogeneities on the solar disk with lifetimes of a few rotations.

Despite a wide-ranging existing literature on SMMF observations, spanning several decades, ultimately, our understanding is limited and the SMMF origin remains a crucial, open question in solar physics. The principle component of the SMMF is commonly assumed to be weak, large-scale magnetic flux, distributed over vast areas over the entire solar disk, rather than from more concentrated regions such as Active Regions (ARs) or sunspots (Severny, 1971; Scherrer et al., 1977a; Xiang & Qu, 2016). However, conversely, Scherrer et al. (1972) found that the SMMF was most highly correlated with only the inner-most one quarter, by area, of the solar disk, which is more sensitive to active latitudes.

In recent literature, Bose & Nagaraju (2018) provided an interesting and novel approach to understanding the SMMF whereby they decomposed the SMMF through feature identification and pixel-by-pixel analysis of full-disk magnetograms. Bose & Nagaraju (2018) concluded that: (i) the observed variability in the SMMF lies in the polarity imbalance of large-scale magnetic field structures on the visible surface of the Sun, (ii) the correlation between the flux from sunspots and the SMMF is statistically insignificant, (iii) and more critically that the background flux dominates the SMMF, accounting for around 89% of the variation in the SMMF. There still remained a strong manifestation of the rotation in the background magnetic field presented by Bose & Nagaraju (2018), however, which is indicative of inho-

mogeneous magnetic features with lifetimes on the order of several solar rotations rather than the shorter-lived, weaker fields usually associated with the large-scale background.

In order to identify the contours of specific features Bose & Nagaraju (2018) used an adaptive thresholding technique on various Solar Dynamic Observatory Atmospheric Imaging Assembly (SDO/AIA) images of the solar disk to create binary masks for different types of features. These masks were then applied to scaled SDO/HMI magnetograms in order to segment which features contributed to the SMMF. Upon a closer inspection of the example magnetogram in Figure 2 of the paper, with over-plotted contours of identified features from SDO/AIA images, there are clearly regions of strong Magnetic Flux Concentrations (MFCs) in the local vicinity of, and connected to, the identified features that lie outside their contour lines and are therefore allocated to the background magnetic field, rather than attributed to the specific features. It seems an obvious statement to suggest that SDO/AIA optical counterparts of the magnetograms will not exactly align with the observed magnetic flux in the magnetograms, as Sun’s the magnetic field is a holistic feature. We expect that the magnetic field will manifest itself differently in the optical observations and the magnetograms, which leads one to believe that the background component in this study could mistakenly contain flux from some of the identified features.

In particular, in their example plot, the contours for sunspots typically only cover the umbra, not accounting for the surrounding penumbra. It is not clear whether this will have a large effect, but certainly we expect that some strong magnetic flux associated with sunspots has been attributed to the background, or other nearby features. One other note; there was a treatment of plages in this work, from additional chromospheric observations, but a separate, specific handling of faculae in the photosphere was absent. Incorporating this could have contributed to the completeness of the study. Furthermore, a decomposition of the identified

background component into regimes of strong and weak field would have provided more clarity on the exact morphology of the SMMF, and would have likely provided evidence to conclude whether flux from AR features were, in fact, incorporated into the background.

Despite these findings, it is known that the strength of the SMMF is weaker during solar minimum, when there are fewer ARs, and stronger during solar maximum, when there are more ARs. This is suggestive that the evolution of ARs underpins the SMMF.

There is another view in the literature which suggests AR flux dominates the SMMF. It was shown earlier by Kutsenko et al. (2017) that a large component of the SMMF may be explained by strong and intermediate flux regions, associated with ARs. Also using a thresholding technique, they showed between 65% to 95% of the SMMF could be attributed to strong and intermediate flux, while the fraction of the occupied area varied between 2% to 6% of the disk area, depending on the chosen threshold for separating weak and strong flux. This finding suggests that strong, long-lived, inhomogeneous MFCs produce the strong rotation signal in the SMMF. Potential sources could be sunspots, plages, faculae, etc. and Kutsenko et al. (2017) discussed that there is an entanglement of strong flux (typically associated with ARs) and intermediate flux (typically associated with network fields and remains of decayed ARs). Disentangling the flux would have provided a more accurate analysis of the SMMF owing to a clearer picture of the main contributor to the SMMF.

The Sun's dynamo and hence magnetic field is directly coupled to the solar rotation. The Sun exhibits latitude-dependent and depth-dependent differential rotation with a sidereal, equatorial period of around 25 days (Howe, 2009). To Earth-based observers, the synodic rotation of the Sun is observed at around 27 days, and the SMMF displays a dominant periodicity of around 27 days due to the solar rotation (Chaplin et al., 2003; Xie et al., 2017; Bose & Nagaraju, 2018). It was also reported by Xie et al. (2017) that the differential solar rotation was observed in

the SMMF with measured rotational periods of  $28.28 \pm 0.67$  days and  $27.32 \pm 0.64$  days for the rising and declining phases, respectively, of all of the solar cycles in their considered time-frame.

On the other hand, Xiang & Qu (2016) utilised ensemble Empirical Mode Decomposition (EEMD) analysis to extract rotational modes in the SMMF and found two rotation periods which are derived from different strengths of magnetic flux elements. They found that a rotation period of 26.6 days was related to a weaker magnetic flux element within the SMMF, while for stronger magnetic flux elements in the SMMF, the measured rotation period was 28.5 days.

Ultimately, to date, our understanding of the SMMF and its origin remains rather limited.

## 1.2 Aims

In this work an investigation of high-cadence (sub-minute) observations of the SMMF, made by Birmingham Solar Oscillations Network (BiSON) (Chaplin et al., 1996, 2005; Hale et al., 2016), was performed. The aim of the investigation was to understand the morphology of the SMMF.

This work provides a frequency domain analysis of the SMMF data, where a model was built up and fit to the power spectrum of the SMMF which allowed us to understand the characteristics of its source(s).

The Rotationally Modulated (RM) signal in the SMMF was clearly observed as several low-frequency peaks in the power spectrum. In addition, the use of the high-cadence data was especially crucial for inferences on components of the SMMF with periods of less than a day at higher frequencies in the power spectrum, with the intention to determine whether the background magnetic field exhibited a stochastically excited component, which evolved on short timescales.

After fitting a model of the power spectrum, we aimed to use simulated data and other sources of SMMF data to aid the clarification of our inferences from BiSON

against other observations.

## 1.3 Data

### 1.3.1 Summary of the Data Set

Chaplin et al. (2003) provided the first examination of the SMMF using data from BiSON, and the work presented in this paper is a continuation of that study.

BiSON is a six-station, ground-based, global network of telescopes attempting to continuously monitor the Sun, which principally makes precise measurements of the LOS velocity of the photosphere due to solar  $p$  mode oscillations (Hale et al., 2016). Through the use of polarising optics and additional electronics, the BiSON spectrometers can measure both the disk-averaged LOS velocity and magnetic field in the photosphere (Chaplin et al., 2003), however, not all BiSON sites measure the SMMF. The observing regime for BiSON is described below.

In this study we focus on the data collected by the Sutherland node, in South Africa, which was also used by Chaplin et al. (2003). Data are sampled on a 40-second cadence, and the SMMF data collected by the Sutherland station pertains the epochs from 01/1992 – 12/2012. Over this period, the duty cycle of solar observations is low because we are using only a single site, and averages to be  $\sim 15.6\%$  of the total epoch.

As a comparison to the BiSON data, SMMF observations were also acquired from the Wilcox Solar Observatory (WSO) (<http://wso.stanford.edu/>) (Scherrer et al., 1977b). The WSO SMMF data are sampled daily from 16/05/1975 – present day, but for comparison with the BiSON SMMF, we only used data over the same temporal range.

The WSO also measures the LOS SMMF using a Babcock-type magnetograph, which allows the measurement of the amount and sense of circular polarisation in the wings in an absorption line (Scherrer et al., 1977a). WSO uses two absorption lines for the measurement of the magnetic field: the Fe I at 5250 Å ( $\lambda 5250$ ) is



used for measurement of the field, and Fe I at 5124 Å( $\lambda 5124$ ) is used to determine the instrument’s zero offset, as this line is magnetically insensitive. Scherrer et al. (1977a) describes that a single, complete observation takes  $\sim 20$  minutes, consisting of four 3-minute integrations. The data provided by WSO is a daily weighted mean of the observations, where the weighting used is the statistical uncertainty and the magnitude of the zero offset measured with the  $\lambda 5124$  line.

### 1.3.2 Obtaining the SMMF from BiSON

There is no catalogued BiSON SMMF data-set, so it was necessary to compute the SMMF from the available BiSON data. To acquire the SMMF from BiSON data, the method as described by Chaplin et al. (2003) was adopted; here we discuss the key aspects.

Each BiSON site employs a Resonant Scattering Spectrometer (RSS) to measure the Doppler shift of the  $^2S_{1/2} \rightarrow ^2P_{1/2}$  line (D1 line) of potassium, at  $\sim 770$  nm (Brookes et al., 1978). A potassium vapour cell placed within a longitudinal magnetic field Zeeman splits the laboratory line into the two allowed D1 transitions (Lund et al., 2017). The intensity of the longer wavelength (red;  $I_R$ ) and shorter wavelength (blue;  $I_B$ ) components of the line may be measured by the RSS almost simultaneously, by using polarising optics to switch between the red and blue wings of the line, to form the ratio given by equation (1.1), which is used as a proxy for the Doppler shift from the LOS velocity of the photosphere (see Brookes et al. (1976, 1978); Elsworth et al. (1995a); Chaplin et al. (2003); Lund et al. (2017)).

$$\mathcal{R} = \frac{I_B - I_R}{I_B + I_R} \quad (1.1)$$

There are known effects which occur when making observations of the entire solar disk at one time, such as LOS Doppler-imaging and limb-darkening (Davies et al., 2014b). Some BiSON stations, that do not measure the SMMF, use optics to spatially scramble incoming sunlight to remove Doppler-imaging effects, to ensure a

more accurate measure of the disk-averaged Sun-as-a-star. Sutherland, however, is not free from these effects, but they are assumed to be small in the analysis.

Photospheric magnetic fields Zeeman split the Fraunhofer line and the Zeeman-split components have opposite senses of circular polarization (Chaplin et al., 2003). Additional polarising optics are used in the RSS to manipulate the sense of circular polarization (either + or -) that is passed through the instrument. The ratio  $\mathcal{R}_+$  or  $\mathcal{R}_-$  is formed, and the ratios  $\mathcal{R}_\pm$  would be equal if there was no magnetic field present.

The observed ratio ( $\mathcal{R}_\pm$ ) may be decomposed as given by equation (1.2); where  $\mathcal{R}_{\text{orb}}$  is the radial component of the Earth’s orbital velocity around the Sun,  $\mathcal{R}_{\text{spin}}$  is the component towards the Sun of the Earth’s diurnal rotation about its spin axis as a function of latitude and time,  $\mathcal{R}_{\text{grs}}$  is from the gravitational red-shift of the solar line due to the Sun’s mass (Elsworth et al., 1995b; Dumbill, 1999). The LOS velocity due to  $p$  mode oscillations are given by  $\delta r_{\text{osc}}(t)$ , and  $\delta r_B(t)$  is due to the magnetic field (+/- from the polarity) (Dumbill, 1999). The effect of the magnetic field on the ratio is shown in Fig. 1.1, and it is clear to see from equation (1.3) that the difference between the opposite magnetic field ratios is twice the magnetic ratio residual.

$$\mathcal{R}_\pm = \mathcal{R}_{\text{orb}} + \mathcal{R}_{\text{spin}} + \mathcal{R}_{\text{grs}} + \delta r_{\text{osc}}(t) \pm \delta r_B(t) \quad (1.2)$$

$$\mathcal{R}_+ - \mathcal{R}_- = 2 \delta r_B(t) \quad (1.3)$$

In fact, the BiSON RSS is measuring the velocity variation on the solar disk, and therefore a calibration from the ratio to a velocity is necessary. We also note the velocity effects due to spin, orbit, and gravitational red-shift significantly dominate the measured LOS velocity over any of the other effects. One method of velocity calibration is achieved by first fitting the daily observed ratio, averaged over both

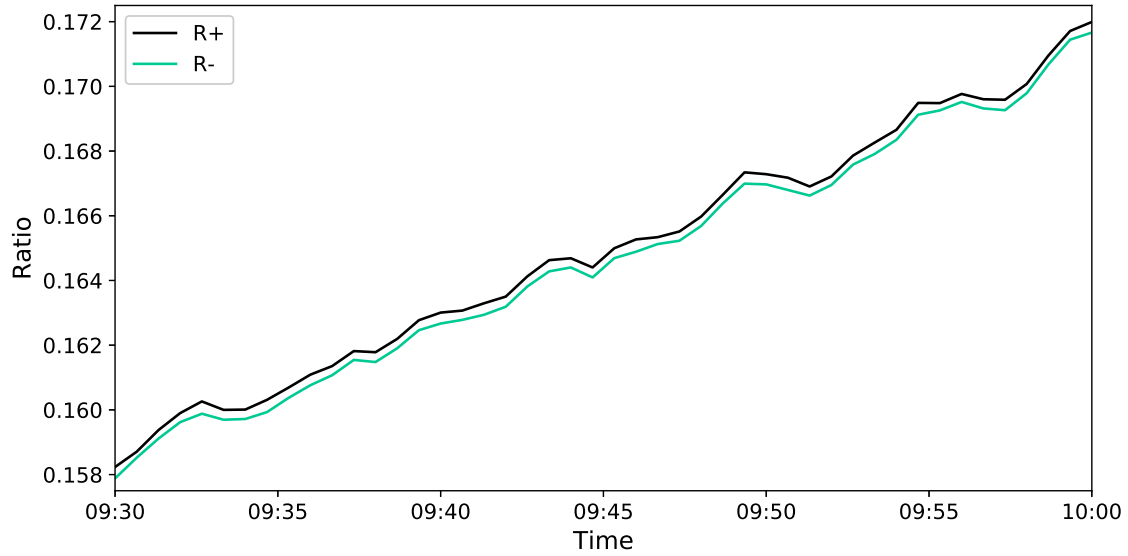


Figure 1.1: An example of the BiSON ratios data over a 30-minute period. The separation between the two ratios is due to the solar mean magnetic field. Other excursions in the individual ratios are due to the other effects measured by the RSS.

magnetic polarities, to a 2nd- or 3rd-order polynomial as a function of velocity, as discussed by Elsworth et al. (1995b). Here we chose to fit the ratio in terms of velocity,  $\mathcal{R}_{\text{calc}}(u)$ , see equation (1.4):

$$\mathcal{R}_{\text{calc}}(u) = \sum_n \mathcal{R}_n u^n \quad (1.4)$$

where:

$$u = v_{\text{orb}} + v_{\text{spin}} \quad (1.5)$$

and  $v_{\text{orb}}$  is the velocity component related to the ratio,  $\mathcal{R}_{\text{orb}}$ ;  $v_{\text{spin}}$  is related to the ratio,  $\mathcal{R}_{\text{spin}}$ ; and  $n$  is the polynomial order.

It is possible to see that through the removal of  $\mathcal{R}_{\text{calc}}(u)$  from the observed ratios, one is left with the ratio residuals of the  $p$  mode oscillations and the magnetic field (see equation (1.6)). Conversion from ratio residuals into velocity residuals uses the calibration given by equation (1.7).

$$\mathcal{R}_{\pm} - \mathcal{R}_{\text{calc}}(u) = \delta r_{\text{osc}}(t) \pm \delta r_{\text{B}}(t) \quad (1.6)$$

$$\delta v(t) = \left( \frac{d\mathcal{R}_{\text{calc}}}{dV} \right)^{-1} \delta r(t) \quad (1.7)$$

In order to finally obtain the SMMF in units of magnetic field, one must combine equation (1.3) and equation (1.7) with the conversion factor in equation (1.8) (Dumbill, 1999), where  $\mu_B$  is the Bohr magneton,  $h$  is Planck's constant,  $c$  is the speed of light, and  $\nu$  is the frequency of the photons, and the entire procedure can be simplified into equation (1.9).

$$K_B = \frac{8}{3} \frac{\mu_B}{h} \frac{c}{\nu} \approx 2.89... \text{ ms}^{-1} \text{ G}^{-1} \quad (1.8)$$

$$B(t) = \frac{1}{2} \left( \frac{d\mathcal{R}_{\text{calc}}}{dV} \right)^{-1} (\mathcal{R}_{+} - \mathcal{R}_{-}) / K_B \quad (1.9)$$

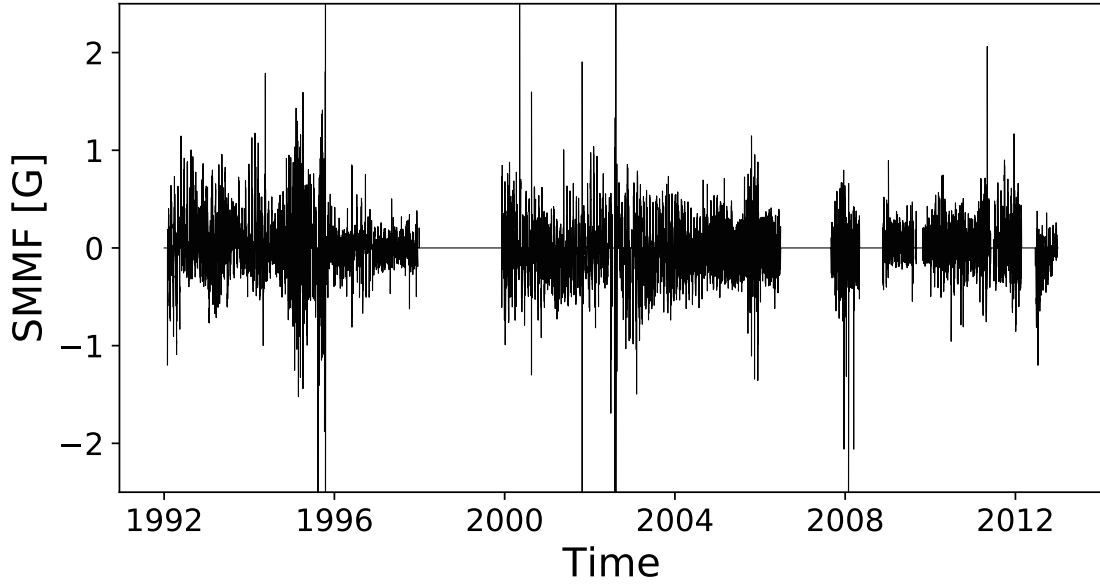
Through the application of this methodology, one acquires the SMMF as shown in Fig. (1.2a). The power spectrum of the SMMF is shown in Fig. (1.2b), and it shows a strong rotational signal at a period of  $\sim 27$  days.

The power spectrum shows a clear set of strong peaks at low frequency, which are due to the persistent rotation signal in the SMMF. The largest peak is the fundamental rotation frequency, and the following peaks are its harmonics.

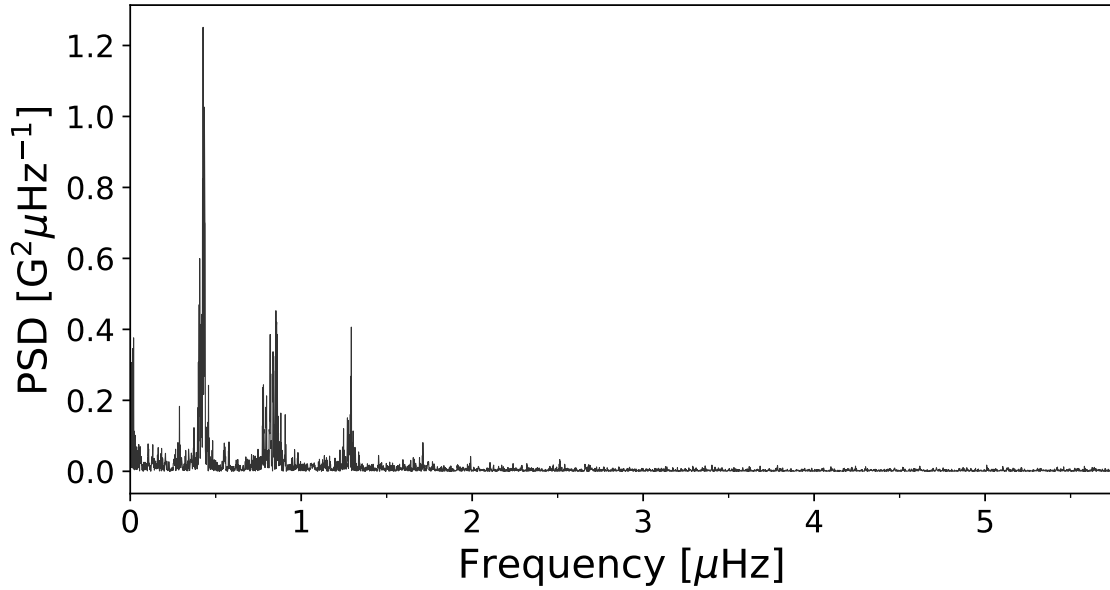
### 1.3.3 Comparison between WSO and BiSON

The relationship between the SMMF measured by the Sutherland BiSON node and the SMMF measured by Stanford WSO was examined. The daily SMMF measured by the Stanford WSO and Sutherland BiSON station are plotted in Fig 1.3.

Figure 1.4 shows the correlation between the two data sets, and also a comparison of their power spectra at low frequencies. The gradient of the line in Fig. 1.4a is  $0.4999 \pm 0.0001$  and informs us that the BiSON SMMF is half of the magnitude of



(a) BiSON SMMF 40-second cadence time series



(b) Power spectral density of the BiSON SMMF

Figure 1.2: (a) 40-second cadence observations of the SMMF from the Sutherland BiSON station between 1992 and 2012. The sense of the field was chosen to match the Chaplin et al. (2003) and the WSO observations, where positive is for a field pointing outwards from the Sun. (b) Power spectrum of the SMMF on a 40-second cadence truncated to  $10\mu\text{Hz}$ , however, the nyquist frequency is  $12.5\text{ mHz}$ .

that observed by WSO. Interestingly Chaplin et al. (2003) stated that the SMMF observed by the Sutherland BiSON station was roughly twice that of WSO, which means there is a self-consistency problem with the calibration of the BiSON SMMF

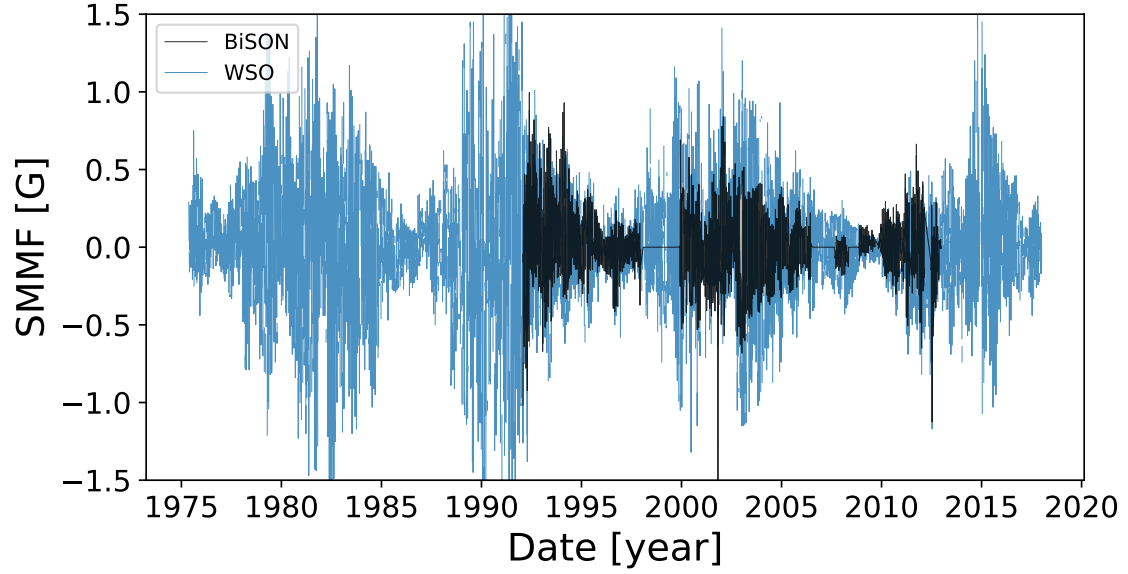


Figure 1.3: Daily averaged SMMF measured by WSO (blue) and by the Sutherland BiSON station (black).

and suggests that there is a factor of 4 difference between the measurements of the SMMF by Chaplin et al. (2003) and in this work.

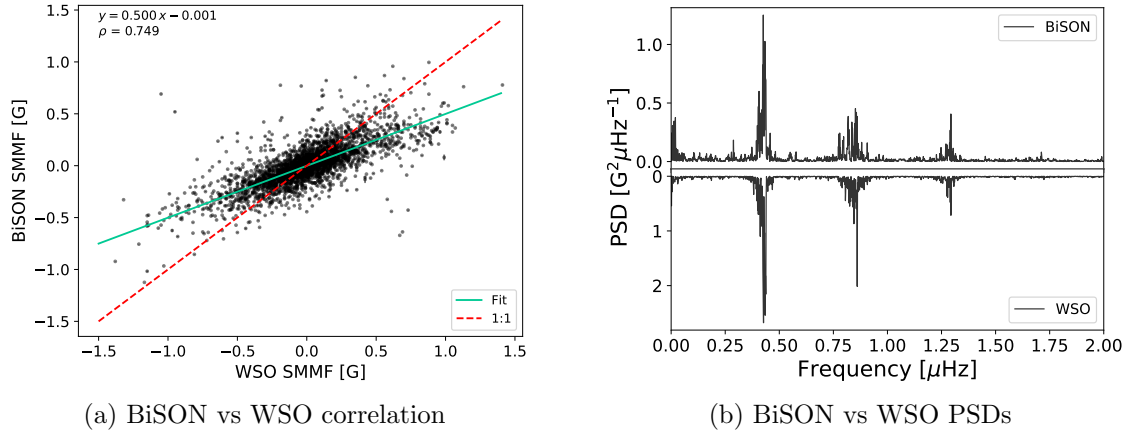


Figure 1.4: Comparisons between the BiSON SMMF data and the WSO SMMF data. (a) The correlation between daily averaged BiSON SMMF and the WSO SMMF. The solid-green line provides the fit to the data, while the dashed-red line shows a 1:1 relation for comparison. (b) Shows a comparison between the power spectra of BiSON and WSO measurements of the SMMF.

A possible reason for the differences between the WSO observations and the BiSON observations may be explained by the formation heights of the lines. Assuming at each level of the solar atmosphere, regions threaded by magnetic field

are in pressure equilibrium with those without any field, then the pressure balance can be expressed by equation (1.10), where  $P_{\text{with}}$  is the gas pressure in regions with magnetic field,  $P_{\text{without}}$  in those without, and  $B^2/2\mu_0$  is the magnetic pressure ( $\mu_0$  = magnetic permeability of free space). This implies that the observed magnetic field scales like  $\sqrt{P}$ .

$$P_{\text{with}} + \frac{B^2}{2\mu_0} = P_{\text{without}} \quad (1.10)$$

Pressure changes exponentially with the scale height,  $H_P$  ( $\sim 100 - 150$  km for the photosphere (Christensen-Dalsgaard et al., 1996)), as described by equation (1.11). Therefore combining both equation (1.10) and equation (1.11), we arrive at equation (1.12).

$$P_2 = P_1 e^{-(h_2 - h_1)/H_P} \quad (1.11)$$

$$B_2 = B_1 e^{-(h_2 - h_1)/(2H_P)} \quad (1.12)$$

Using a Non-Local Thermal Equilibrium (NLTE) simulation to model the spectrum of solar magnetic features (see Figure 1.5, and assuming for some slight calibration issues and Doppler shifting, we might suppose that the formation height of the BiSON line (in vacuum) is around 50 km, and for the WSO line (in vacuum), around 150 km. This would mean that  $B_{\text{WSO}} \approx 0.6 B_{\text{BiSON}} - 0.7 B_{\text{BiSON}}$  which disagrees with our observations and the comparison in Figure 1.4, but agrees more favourably with Chaplin et al. (2003).

[Need to decide still how to neatly handle the discrepancy between old paper, this work, and WSO...]

Finally, we can see quite clearly that the two power spectra align very closely, as shown in Fig. 1.4b, and that both spectra appear to display an asymmetric peak shape, with a negative asymmetry. The WSO power spectrum does also appear to

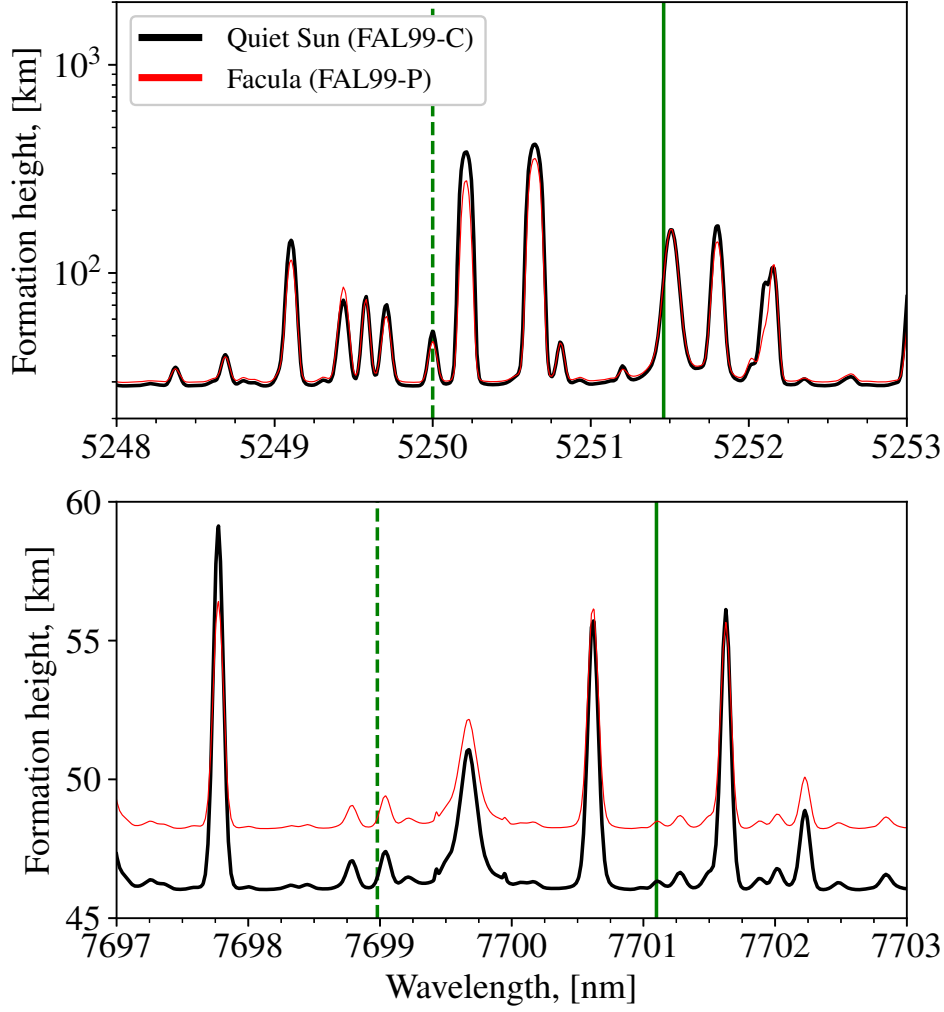


Figure 1.5: Formation heights of emission lines over the wavelength range used for WSO observations (top) and for BiSON observations (bottom). The vertical lines show the wavelengths of the emission lines used for observations in air (dashed) and in vacuum (solid). This plot was provided in private communication courtesy of Rinat Tagirov using the NESSY code.

display a lower degree of noise compared to BiSON.

## 1.4 Methodology

### 1.4.1 Identifying Features in the SMMF Power Spectrum

The full power spectrum of the 40-second cadence SMMF is shown in Figure 1.6, covering a frequency range up to the Nyquist frequency of 12.5 mHz with a resolution of 1.516 nHz.



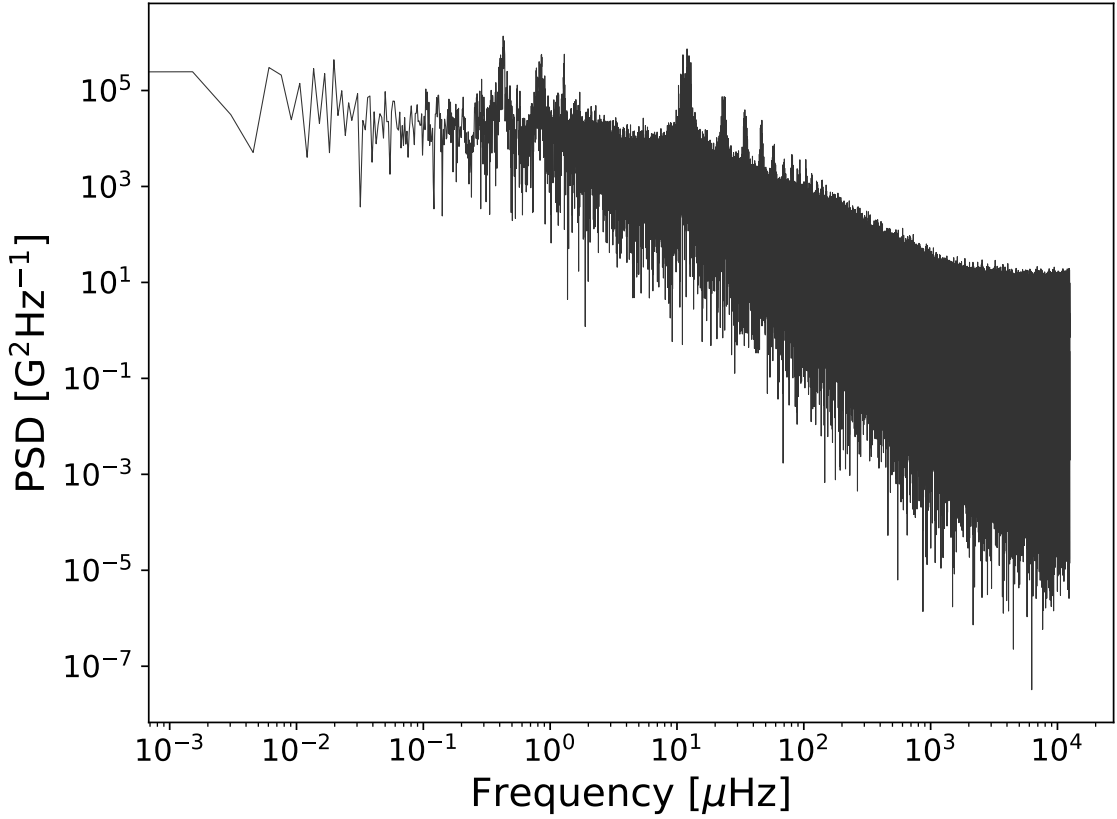


Figure 1.6: Full power spectrum of the BiSON SMMF on a logarithmic scale up to the Nyquist frequency.

There are a number of features in the power spectrum. First, the peaks between  $0.1 - 2.0 \mu\text{Hz}$  are a manifestation of a persistent rotational signal the SMMF. The distinct set of peaks indicates the existence of a long-lived, inhomogeneous, RM source. The SMMF signal exhibits a quasi-coherent behaviour in the time domain, and based on the comparatively short timescales for the emergence of magnetic features compared to their slow decay (i.e. hours–days compared to weeks–months) (Zwaan, 1981; Harvey & Zwaan, 1993; Hathaway & Choudhary, 2008; Dacie et al., 2016), we assume the evolution of the RM component with time is a sudden appearance and a long, exponential decay.

As we have 40-second cadence observations of the SMMF, we were able to investigate the power spectrum up to a high Nyquist frequency. This was critical in uncovering a red-noise-like component in the power spectrum. This component

could arise from continuously evolving, short-lived regions of magnetic field linked to magneto-convection, akin to a random walk, which we will dub the Stochastic Background (SB) component. Analogous to the SB, is the granulation signal observed in the Doppler-velocity measurements of the solar surface (Basu & Chaplin, 2017).

In addition, at low-frequency there is power associated with instrumental noise and solar activity, and at very-high frequency shot-noise is captured which sets the lower limit in power in the spectrum.

There are also side-band features in the power spectrum at multiples of  $1/\text{day} \sim 11.57 \mu\text{Hz}$ . The side-bands are a well-known phenomena in ground-based helioseismology. They arise from gaps in the data which are a consequence of making single-site, ground-based observations of the Sun.

The duty cycle of the BiSON observations is very low, at around  $\sim 15\%$ , therefore it was important to take into consideration the effect that gaps in the data have on the power spectrum. Gaps in the data cause an aliasing of power from actual signal frequencies spread to other frequencies in the spectrum, and the nature of the aliasing depends on the properties of the window function of the observations. It is also possible that the SB component is an effect of power aliasing due to the low duty cycle of the data. Hence, before modelling the power spectrum, the window function was well-characterised.

Through understanding how the duty cycle of the observations affected the power spectrum informed the way we finally parametrised the full model of the power spectrum.

### 1.4.2 Parameterisation of the SMMF Power Spectrum

In the frequency domain, each of the RM peaks models well as a Lorentzian distribution, similar to peak-bagging modes of solar oscillation (Handberg & Campante, 2011; Davies et al., 2014a), which is due to the quasi-coherent nature of the source.

The exponential decay of the RM SMMF source gives width to the peaks in the power spectrum, which we can measure to infer their lifetime.

A single, symmetric Lorentzian peak can be modelled by equation (1.13), where  $\nu$  is frequency,  $A_n$  is the mode amplitude of the RM component,  $\Gamma$  is the mode line-width, and  $\nu_n$  is the frequency of the mode.

$$L_n(\nu; \Gamma, A_n, \nu_n) = \frac{2A_n^2}{\pi\Gamma} \left( 1 + \left( \frac{\nu - \nu_n}{\Gamma/2} \right)^2 \right)^{-1} \quad (1.13)$$

Upon closer inspection of the power spectrum it is possible to see that the peaks appear to exhibit an asymmetric shape (see Figure 1.2 and Figure 1.4b). Taking inspiration from (Howe et al., 2020), it is possible to allow for asymmetry in the Lorentzian peak, which is controlled by the asymmetry parameter,  $\alpha$ , in equation (1.14):

$$L_n(\nu; \Gamma, A_n, \nu_n) = \frac{2A_n^2}{\pi\Gamma(\nu)} (1 + (2X(\nu))^2)^{-1} \quad (1.14)$$

where

$$X(\nu) = (\nu - \nu_n)/\Gamma(\nu) \quad (1.15)$$

$$\Gamma(\nu) = 2\Gamma/[1 + \exp^{-\alpha(\nu - \nu_n)}]. \quad (1.16)$$

This parameterisation of the asymmetric Lorentzian stops any of the power from becoming negative. In the limit where  $\alpha \rightarrow 0$ , we see that  $\Gamma(\nu) \rightarrow \Gamma$ , thus the asymmetric expression equates to the symmetric expression.

The model function used to describe the RM signal in the power spectrum is given by equation (1.17); the sum of  $N$  Lorentzian-peaks. The subscript,  $n$ , describes a single peak in the power spectrum; in implementing the model we constrain the mode frequencies such that they must be integer values of  $\nu_0$ :  $\nu_n = n\nu_0$ . This

means that we define a single rotation frequency only, and subsequent peaks are harmonics. It is worth noting explicitly that this function assumes the line-width of each Lorentzian peak is the same; only their amplitudes and central frequency differ.

$$P(\nu) = \sum_{n=1}^N L_n(\nu; \Gamma, A_n, \nu_n) \quad (1.17)$$

When modelling the power spectrum we attempted with both the symmetric and asymmetric Lorentzian expressions, independently, to determine whether there is a necessity for the extra asymmetry parameter.

Through this formulation we can measure the lifetime of the RM component ( $L$ ), as it is related to the line-width of the peak by equation (1.18).

$$\Gamma = (\pi L)^{-1} \quad (1.18)$$

The low-frequency power can be incorporated into the model via the inclusion of a zero-frequency centred Lorentzian, i.e. Harvey-function, given by equation (1.19); where  $\sigma$  is the characteristic amplitude of the low frequency signal, and  $\tau$  describes the characteristic timescale of the excursions around zero.

$$H(\nu; \sigma, \tau) = \frac{4\sigma^2\tau}{1 + (2\pi\nu\tau)^2} \quad (1.19)$$

The SB component can also be modelled using the Harvey-function, where  $\sigma$  is the characteristic amplitude of the red-noise signal and  $\tau$  is its characteristic timescale.

Finally, the high frequency power is accounted for by the inclusion of a constant offset due to shot-noise,  $c$ .

When modelling the power spectrum we used the affine-invariant Markov Chain Monte Carlo (MCMC) sampler **emcee** (Foreman-Mackey et al., 2013) to explore the posterior parameter space. The chains are not independent within **emcee**, therefore

convergence was interrogated using the integrated autocorrelation time, to quantify the effects of sampling error on the results and to ensure we used a sufficient number of effective samples.

### 1.4.3 Comparison with the WSO SMMF

To provide comparative results on the inferences from the BiSON SMMF, we repeated the analysis on the power spectrum of the WSO SMMF. The WSO data are only provided on a daily cadence, hence the Nyquist frequency is lower than for BiSON, at  $\sim 5.79 \mu\text{Hz}$ , and it was not possible to observe the SB component.

The same parametrisation as outlined above was relevant to the modelling of the features in the WSO Power Spectral Density (PSD), and the RM peak were fit using a model with symmetric Lorentzian peaks and separately with asymmetric Lorentzian peaks.

## 1.5 Results

### 1.5.1 Investigation of the Window Function

Daily gaps in the data cause some power from the low-frequency RM component in the power spectrum to be aliased to higher frequencies, specifically to harmonics of the frequency of the gaps in the data. In this case there are daily gaps, hence power is aliased to a frequency of  $1/\text{day} \sim 11.57 \mu\text{Hz}$  and its harmonics.

The mode frequency (and harmonics) of the RM component are located near zero ( $\nu_0 \sim 0.4 \mu\text{Hz}$ ). We are usually only interested in the real, positive frequencies but due to their close proximity to zero, they are reflected back as a product of the aliasing and hence there are negative and positive side-bands in the complete power spectrum. When considering the aliased power, both the positive and negative side-bands must be taken into account. The aliased power is located at frequencies defined in equation (1.20), where  $i$  denotes the side-band number, and  $n$  denotes the harmonic of the mode. The locations of side-bands are shown clearly to obey

equation (1.20) in the SMMF power spectrum show in Fig. 1.7.

$$\nu_{n,i} = i \left( \frac{1}{\text{day}} \pm \nu_n \right) \quad (1.20)$$

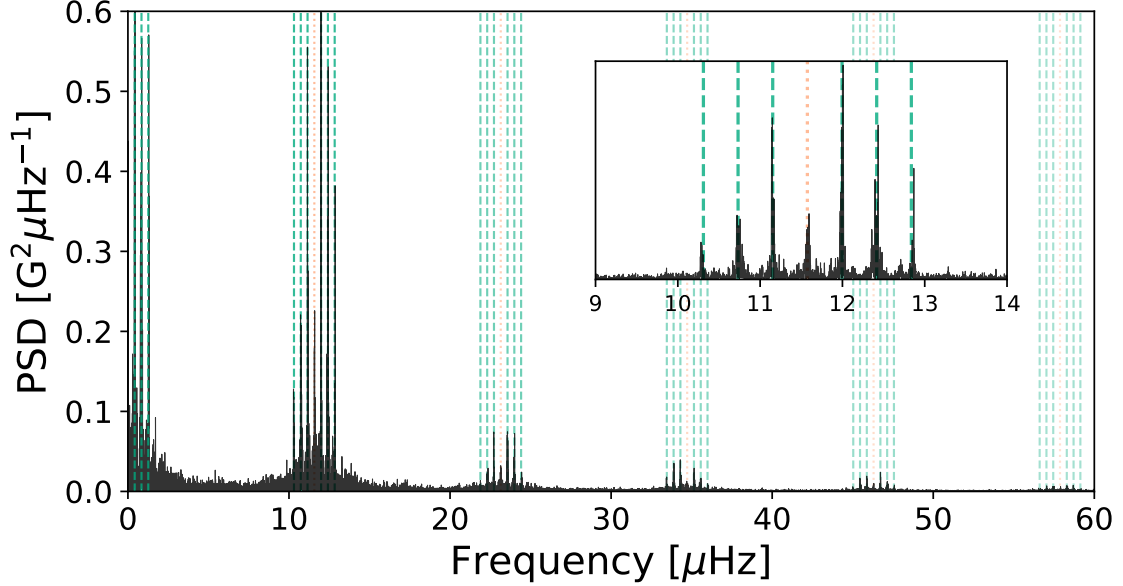


Figure 1.7: Locations of aliased power in side-band peaks. The orange, dotted-lines show the locations of frequencies at multiples of 1/day. The green, dashed-lines show the locations of the side-band peaks – harmonic frequencies reflected around multiples of 1/day. The inset shows a zoom of one set of side-band peaks around 1/day.

It is clear that we could therefore have used the predicted locations of the aliased power and incorporated them into the model for the full power spectrum. This would, however, have required us to explicitly model some  $\sim 1100$  groups of side-bands in order to cover this effect over the entire frequency range, and each group would have required a unique parameter to control the fraction of power that was contributed to the full PSD. It would have become computationally expensive to model each aliased peak and there would certainly have been room for degeneracy issues to occur.

An alternative approach was to utilise the power spectrum of the window function itself. To do this the Fourier transform of the window function describing the duty cycle of observations was computed (i.e.  $|\mathcal{F}[g(t)]|^2$ ), where the duty cycle function,

$g(t)$ , is given by equation (1.21). In Figure 1.8 the power spectrum of the window function is shown.

$$g(t) = \begin{cases} 1 & \text{for } |B(t)| > 0 \\ 0 & \text{for } |B(t)| = 0 \end{cases} \quad (1.21)$$

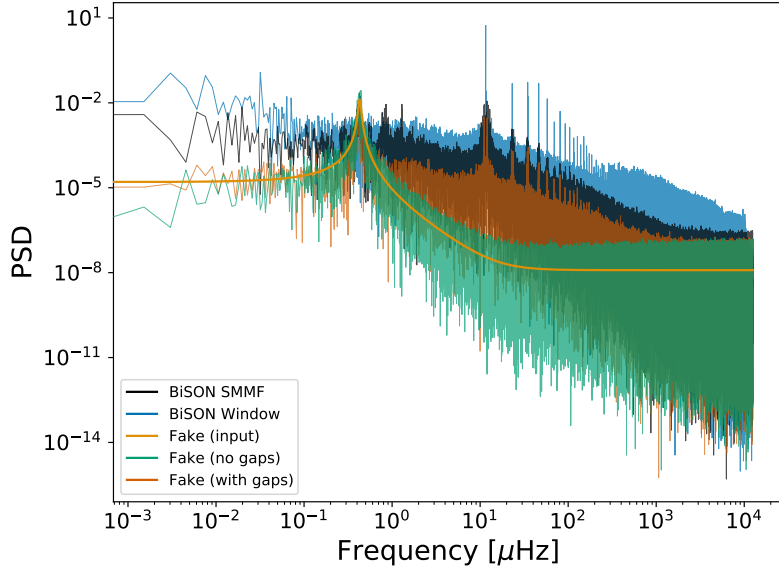
Furthermore, to demonstrate the effect of the window function on the power spectrum, an artificial spectrum was simulated with a single Lorentzian peak, following equation (1.17). By computing the inverse Fourier transform, an artificial time-series was generated over the same epoch as the BiSON SMMF observations. We were then able to examine the effects of injecting gaps into the data which were concurrent with the BiSON SMMF gaps.

As well as the power spectrum of the window function, Figure 1.8 also shows the noiseless peak used to generate the fake data and the power spectra of the artificial data with and without the injected gaps. The power spectrum of the BiSON SMMF data is also plotted for comparison.

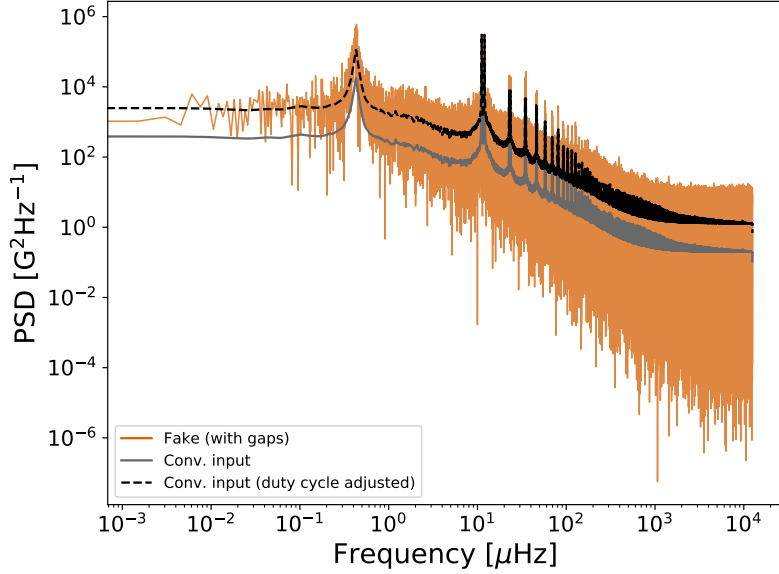
It is strikingly clear from Figure 1.8 that the shape of the spectrum of the window function has a remarkable resemblance to the BiSON SMMF spectrum and the output of the artificial spectrum with gaps injected. This demonstrates that the periodic window function, with such a low duty cycle, has a dominating effect on the power spectrum of the input signal which not only produces the diurnal sidebands, but also a broadband spread of the power.

Due to the broadband shape of the window function power spectrum compared to the BiSON SMMF, it appears that there is actually no red-noise-like, SB component in the SMMF; it is instead a manifestation of the periodic gaps in the data. There is still a necessity for a low-frequency Harvey function to describe the power close to zero.

To analytically understand this effect, we can express the time series of observed data ( $y(t)$ ) as a multiplication of the uninterrupted, underlying signal ( $f(t)$ ) with



(a) Black line: BiSON SMMF PSD; blue line: power spectrum of the window function; green and dark-orange lines: the power spectrum of the artificial data without and with gaps, respectively; light orange line: the input peak used to generate the artificial data over-plotted. The lines have been offset for clarity.



(b) Dark-orange line: the power spectrum of the artificial data with gaps; solid-grey line: input PSD convolved with the window function; dashed-black line: input PSD convolved with the power spectrum and adjusted for the duty cycle.

Figure 1.8: (a) The effect on the power spectrum due to periodic gaps in the data. (b) The effect of the convolution between the window function and the input power spectrum used to make the fake data, highlighting the need to correctly adjust the power for the duty cycle.



the window function ( $g(t)$ ), as given by equation (1.22).

$$y(t) = f(t) g(t) \quad (1.22)$$

In the frequency domain, as the Fourier transform of a product becomes the convolution of the transformed components. It is possible to express the observed power spectrum of data with periodic gaps in terms of the window function and the gap-free power spectrum, given in equation (1.23)

$$P'(\nu; \mathbf{a}) = P(\nu; \mathbf{a}) * |\mathcal{F}[g(t)]|^2 \quad (1.23)$$

Therefore to model the observed power spectrum in a robust manner, which takes into account the intricacies caused by gaps in the data, we used a model which was formed of a model power spectrum,  $P(\nu; \mathbf{a})$ , convolved with the Fourier transform of the window function describing the duty cycle of observations ( $|\mathcal{F}[g(t)]|^2$ ), i.e. a model described by equation (1.23), where

$$P(\nu; \mathbf{a}) = \sum_{n=1}^N L_n(\nu; \Gamma, A_n, \nu_n) + H(\nu; \sigma, \tau) + c. \quad (1.24)$$

Care was taken to ensure Parseval's theorem was obeyed, and no power was lost or gained from the convolution operation. The likelihood of the resulting model from the convolution,  $P'(\nu; \mathbf{a})$ , was then maximised to give the best fitting parameters.

We demonstrated the convolution process by performing the convolution between the noiseless peak used to generate the artificial data and the window function. The result of this is shown in Figure 1.8b. Due to method adopted for the convolution, the overall power was reduced as can be seen by the solid-grey line in Figure 1.8b. It was therefore necessary to adjust the resultant power spectrum by the duty cycle factor, i.e.  $\sim 15\%$  for BiSON 40-s cadence observations, which produced the dashed-black line in Figure 1.8b, which aligns with the power spectrum of the artificial data with gaps.

To further demonstrate the effects of the convolution process during the modelling, we fit a model of a single Lorentzian peak, plus a shot-noise background, to the gap-free fake PSD (without the convolution) and the fake PSD using the gaps (requiring the convolution). The modelling was performed using the affine-invariant MCMC sampler `emcee` (Foreman-Mackey et al., 2013) to explore the posterior parameter space, using 6000 iterations on 50 chains. The results of this fit are summarised in Table 1.1.

Table 1.1: Model parameter values for the generation of artificial data, and the median posterior values for the fit to the power spectra generated with and without the gaps in the data. Numbers in brackets denote uncertainties on the last 2 digits, and all uncertainties correspond to the 68% credible intervals either side of the median.

Parameter	Input	Fit (no gaps)	Fit (gaps)	Unit
$\nu_0$	0.42867	$0.4277^{(+18)}_{(-18)}$	$0.4261^{(+03)}_{(-03)}$	$\mu\text{Hz}$
$\Gamma$	0.030	$0.0279^{(+37)}_{(-36)}$	$0.0340^{(+06)}_{(-06)}$	$\mu\text{Hz}$
$A$	100.0	$101.2^{+7.3}_{-6.0}$	$282.56 \pm 0.25$	mG
$c$	0.20	$0.1872^{(+03)}_{(-03)}$	$1.2009^{(+08)}_{(-08)}$	$\text{G}^2\text{Hz}^{-1}$

There were several points uncovered about the convolution process in this fitting procedure that we had to take into consideration. Firstly, we found agreement with the effect on the total power observed in Figure 1.8. The median posterior values of the amplitude and shot noise parameters were affected by the duty cycle, compensating for the effect on the power, which resulted in the amplitude posterior being too large by a factor of the square-root of the duty cycle ( $\sim \sqrt{0.15}$ ) and the shot noise being too large by a factor of the duty cycle ( $\sim 0.15$ ). This again highlights the necessity to incorporate the duty cycle into the convolution to ensure Parseval’s theorem is obeyed. After the correction, the median posterior values for the amplitude and noise become:  $111.7 \pm 0.1$  mG and  $0.1876^{(+01)}_{(-01)} \text{G}^2\text{Hz}^{-1}$ , respectively, which are in-line with the expected values.

In addition, we found that the width of the posterior distributions for the parameters were generally smaller as a result of the convolution process. We therefore observed that the likelihood evaluation, when using the convolved model, does not

fully take into account the correlated noise on the power spectrum. To perform the full likelihood evaluation, with the correlated noise, requires large-data computational linear algebra (i.e. the inversion of an  $N$ -by- $N$  diagonal-constant/Toeplitz matrix, where  $N$  is the size of data); unfortunately the process of fully accounting for the correlated noise in this scenario was too computationally expensive, due to the large data set with  $> 10^6$  data points. After the corrections for Parseval’s theorem, we noticed the  $\nu_0$  and  $\Gamma$  posterior widths appeared to be reduced by a factor of approximately the duty cycle. For the amplitude and shot noise this is not the case, however. We note here that our ability to resolve the model parameters is well represented in the case where the convolution wasn’t performed; thus, we assumed the for  $\nu_0$  and  $c$ , we have an accuracy of  $\sim 0.5\%$  each; for  $\Gamma$ , an accuracy of  $\sim 15\%$ ; for  $A$ , an accuracy of  $\sim 10\%$ . As we cannot directly account for the effect of posterior width shrinkage, we note these factors, which helps understand how the convolution affected our ability to measure the spectrum of the BiSON SMMF.

From this exercise we learned that during the modelling of the BiSON (and WSO) power spectra, we needed to account for the duty cycle to ensure no loss of power from the convolution process. We have also learnt that the likelihood evaluation does not properly take into consideration the effect of the correlated noise in the power spectrum, but it is too computationally expensive to account for.

### 1.5.2 Modelling the BiSON Power Spectrum

As there were many data points in the power spectrum, each likelihood calculation was computationally expensive. In order to reduce the required computation, the BiSON power spectrum was cut at a frequency of  $7000 \mu\text{Hz}$ , as at very high frequency, the spectrum purely represents the noise in the SMMF, and it was deemed as a sufficient limit to still fully converge on the shot noise parameter.

We have shown the likelihood evaluation doesn’t fully take into account the correlated noise due to the convolution, and doing so would have been too expensive

to compute; hence, the pragmatic approach was to ignore the effect of the correlated noise in the convolution on the likelihood calculation.

The BiSON power spectrum was modelled against equation (1.23) (which used equation (1.24) with  $N = 4$  peaks) using the affine-invariant MCMC sampler **emcee** (Foreman-Mackey et al., 2013) to explore the posterior parameter space, using 7000 iterations on 50 chains, which was shown to provide a sufficient number of independent samples for convergence. In the modelling we used non-informative, uniform prior information, providing reasonable boundaries on each parameter, as detailed below.

$$\begin{aligned}
\nu_0 &\sim \mathcal{U}(0.38, 0.50) \mu\text{Hz} \\
\Gamma &\sim \mathcal{U}(0.00, 0.11) \mu\text{Hz} \\
A_1 &\sim \mathcal{U}(100, 350) \text{ mG} \\
A_2 &\sim \mathcal{U}(50, 200) \text{ mG} \\
A_3 &\sim \mathcal{U}(20, 150) \text{ mG} \\
A_4 &\sim \mathcal{U}(10, 100) \text{ mG} \\
\sigma &\sim \mathcal{U}(0.01, 500) \text{ mG} \\
\tau &\sim \mathcal{U}(0.10, 200) 10^6 \text{ s} \\
c &\sim \mathcal{U}(10^{-3}, 10^2) \text{ G}^2 \text{ Hz}^{-1} \\
\alpha &\sim \mathcal{U}(-500, 0)
\end{aligned}$$

In Table 1.2 the median values of marginalised posterior distributions for each of the model parameters are displayed. Reported uncertainties on the parameters correspond to the  $1\sigma$  (68%) credible intervals either side of the median. We note that we have previously shown the convolution results in a shrinkage in the width of

the posterior distributions and thus here we are presenting an underestimation of the uncertainties.

Table 1.2: Median values of the marginalised posterior distributions for each model parameter in the fit to the BiSON power spectrum, adjusted for the duty cycle factor ( $\sim 0.156$ ) in the convolution process. Numbers in brackets denote uncertainties on the last 2 digits, and all uncertainties correspond to the 68% credible intervals either side of the median.

Parameter	40-s symm.	40-s asymm.	Unit
$\nu_0$	$0.42699^{(+13)}_{(-13)}$	$0.42778^{(+14)}_{(-14)}$	$\mu\text{Hz}$
$\Gamma$	$0.02639^{(+49)}_{(-48)}$	$0.03163^{(+71)}_{(-71)}$	$\mu\text{Hz}$
$A_1$	$166.0 \pm 2.0$	$178.9 \pm 1.2$	mG
$A_2$	$115.9 \pm 2.3$	$129.0 \pm 1.2$	mG
$A_3$	$83.2 \pm 2.7$	$93.5 \pm 1.2$	mG
$A_4$	$32.6 \pm 4.3$	$38.9 \pm 1.9$	mG
$\tau$	$51.8^{+3.9}_{-3.7}$	$62.7^{+4.9}_{-4.6}$	days
$\sigma$	$83.4 \pm 3.5$	$79.1 \pm 1.4$	mG
$c$	$0.2103^{(+09)}_{(-09)}$	$0.2102^{(+01)}_{(-01)}$	$\text{G}^2\text{Hz}^{-1}$
$\alpha$	—	$-119.8^{+8.0}_{-7.9}$	—

As the asymmetry parameter converged reasonably within the prior bounds we therefore deduced that the extra parameter was necessary, and the model utilising asymmetric Lorentzian peaks was a better fit to the data than the model with symmetric Lorentzian peaks. The convolved model of the data, using asymmetric Lorentzian peaks, is shown in Figure 1.9, over-plotted on top the BiSON SMMF power spectrum.

The central frequency of this model,  $\nu_0$  implies a rotation period of  $27.06^{+0.01}_{-0.01}$  days, and accounting for sidereal rotation,  $25.19^{+0.01}_{-0.01}$  days. The rotation period measured is in agreement with other literature values for the rotation signal in the SMMF (Chaplin et al., 2003; Xie et al., 2017). We note here again the convolution process shrinks the posterior distributions and we expect that the true uncertainties on the frequency of rotation and thus the period should be, in fact,  $\sim 0.5\%$  (i.e. approx.  $\pm 0.1$  days).

According to the model for differential rotation given by Snodgrass (1983) and Brown et al. (1989), the measured rotation period implies the RM component of

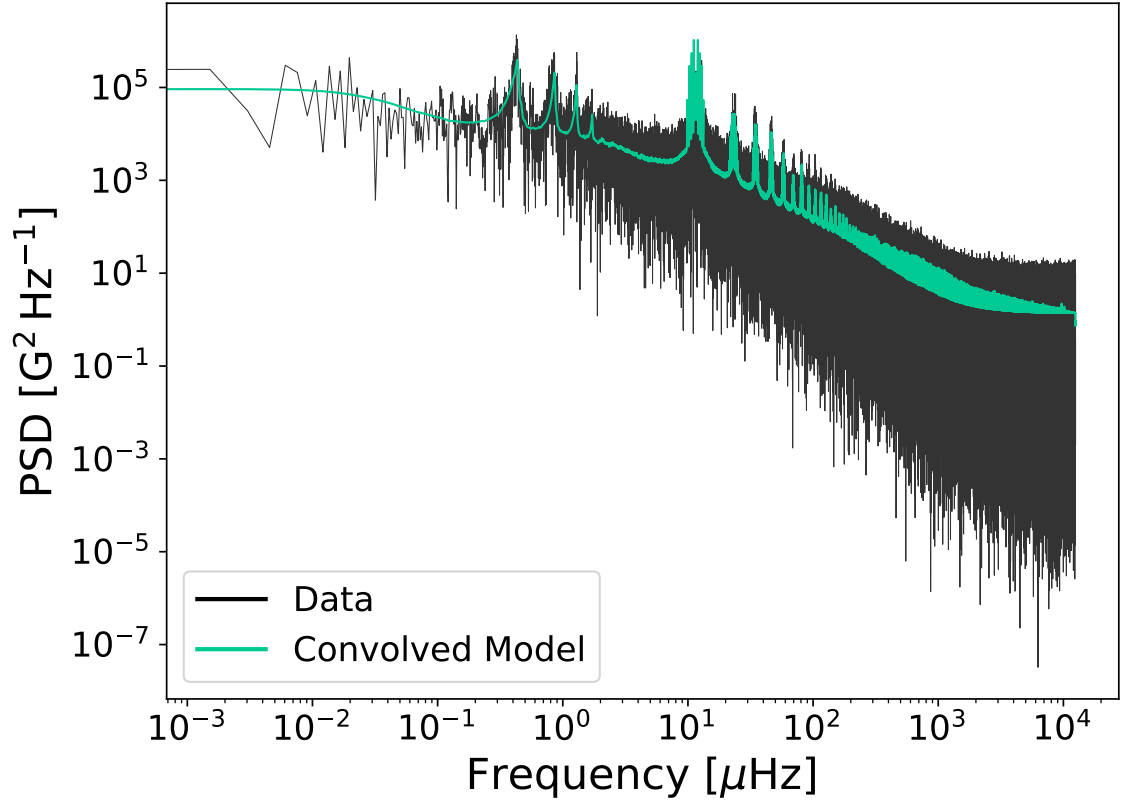


Figure 1.9: Full, modelled power spectrum of the BiSON SMMF on logarithmic axes. The data are displayed in black and the convolved model using asymmetric Lorentzian peaks is shown in green.

the SMMF is sensitive to a time-averaged latitude of around  $11^\circ$ . This latitude is consistent with the latitudes spanned by sunspots and ARs over the solar activity cycle (Maunder, 1904; McIntosh et al., 2014; Thomas et al., 2019), and particularly during the declining phase of the solar cycle. This strongly implies that the origin of the RM component of the SMMF is linked to ARs and MFCs.

Furthermore, from the measured line-width of the Lorentzian peaks, we have calculated the lifetime of the RM component using equation (1.18). The line-width suggests a lifetime of  $116.5 \pm 2.6$  days, which is in the region of  $\sim 16.5$  weeks. The typical lifetime of ARs and sunspots is usually on the order of weeks to months, dependent on their size (Zwaan, 1981; Schrijver & Harvey, 1994; Howard, 2001; Hathaway & Choudhary, 2008; van Driel-Gesztelyi & Green, 2015), therefore we have measured a lifetime of the RM component which is consistent with the lifetime

of ARs and sunspots. This again suggests that the source of the signal is linked to active regions of magnetic field or similar MFCs. We note, in addition, the convolution process shrinks the posterior distributions and we expect that the true uncertainties on the width and thus the lifetime should be, in fact,  $\sim 15\%$  (i.e. approx.  $\pm 15$  days).

Taking into account the work performed by Bose & Nagaraju (2018), which showed evidence to suggest sunspots did not contribute to the SMMF, and our concerns with their methodology, we cautiously do not specify that sunspots are the strong RM source of the SMMF; however, this can still not be ruled out altogether. The method of identifying ARs or strong MFCs in magnetograms by Bose & Nagaraju (2018) potentially mis-identified regions of magnetic flux associated with ARs and MFCs as background flux and it is possible that they do contribute to the SMMF. By comparison with the work carried out by Kutsenko et al. (2017), the work performed in this project agrees that the SMMF is dominated by features with properties in-line with spots, ARs, and MFCs, i.e. long-lived and making up a small fraction of the solar disk, confined to active bands of latitude.

With all this considered, we state that our investigation of the BiSON SMMF indicates the SMMF has its origin in the vicinity of ARs and other concentrations of strong flux that are long-lived on the solar disk and exist in active latitudes. Whether or not specifically this is due to spots or other MFCs will require further work on the magnetogram thresholding techniques investigating the SMMF.

### **1.5.3 Comparison to the WSO Power Spectrum**

When modelling the WSO power spectrum, although the duty cycle of the WSO observations over the same epoch as BiSON observations was  $\sim 78\%$ , therefore there was less of an effect from the window function on the observations, the power spectrum was modelled using the convolution with the window function, as per the BiSON power spectrum. As, compared to the duty cycle of BiSON the WSO duty

is closer to 100%, we expect the effect of the convolution to be less significant on the widths of the posterior distributions for each parameter.

The BiSON power spectrum was modelled against equation (1.23) (which used equation (1.24) with  $N = 3$  peaks) using the affine-invariant MCMC sampler **emcee** (Foreman-Mackey et al., 2013) to explore the posterior parameter space, using 10000 iterations on 50 chains. The chains are not independent within **emcee**, therefore convergence was interrogated using the integrated autocorrelation time, to quantify the effects of sampling error on the results and to ensure a sufficient number of effective samples were used.

In Table 1.3 the median values of marginalised posterior distributions for each of the model parameters are displayed. Reported uncertainties on the parameters correspond to the  $1\sigma$  (68%) credible intervals either side of the median. The effect of posterior width shrinkage in these results seems much less of a concern, as the  $1\sigma$  uncertainties are on the same order as the results not using a convolved model in Table—1.1. The convolved model of the data, using asymmetric Lorentzian peaks is shown in Figure 1.10 over-plotted on top the BiSON SMMF power spectrum.

Table 1.3: Median values of the marginalised posterior distributions for each model parameter in the fit to the WSO power spectrum, adjusted for the duty cycle factor ( $\sim 0.778$ ) in the convolution process. Numbers in brackets denote uncertainties on the last 2 digits, and all uncertainties correspond to the 68% credible intervals either side of the median.

Parameter	24-hr symm.	24-hr asymm.	Unit
$\nu_0$	$0.4273^{(+05)}_{(-05)}$	$0.4290^{(+04)}_{(-05)}$	$\mu\text{Hz}$
$\Gamma$	$0.0209^{(+16)}_{(-15)}$	$0.0210^{(+16)}_{(-15)}$	mG
$A_1$	$134.4^{+3.2}_{-3.3}$	$137.0^{+3.4}_{-3.5}$	mG
$A_2$	$120.7 \pm 3.4$	$124.8^{+3.5}_{-3.6}$	mG
$A_3$	$73.7 \pm 3.5$	$77.4 \pm 3.8$	mG
$\tau$	$22.5^{+10.1}_{-6.9}$	$23.7^{+11.1}_{-7.3}$	$10^6\text{s}$
$\sigma$	$52.1^{+4.7}_{-4.4}$	$51.5^{+4.6}_{-4.5}$	mG
$c$	$11.4^{+17.8}_{-8.5}$	$12.0^{+18.6}_{-8.9}$	$\text{G}^2\text{Hz}^{-1}$
$\alpha$	—	$-61.7^{+13.3}_{-15.3}$	—

The fit to the WSO power spectrum using asymmetric Lorentzian profiles produces results that are close to those measured with the BiSON power spectrum. The



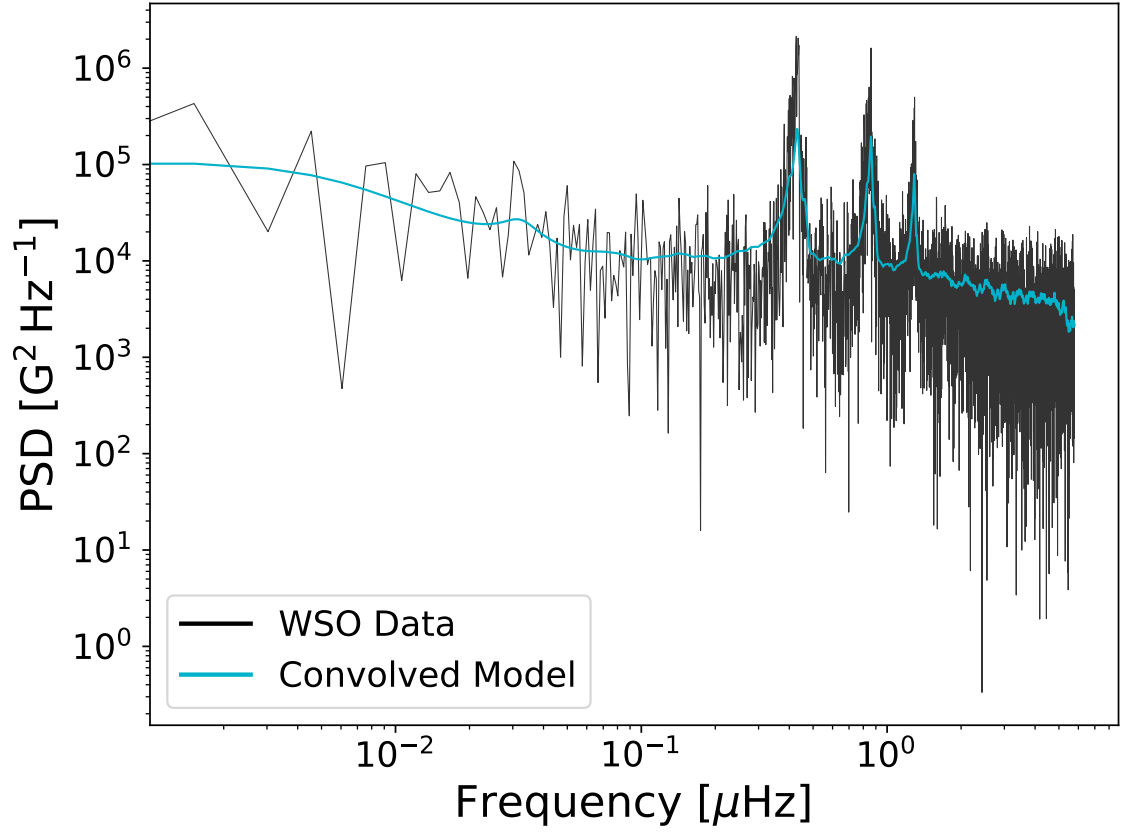


Figure 1.10: Full, modelled power spectrum of the WSO SMMF on logarithmic axes. The data are displayed in black and the convolved model using asymmetric Lorentzian peaks is shown in blue.

rotation period is in agreement with that measured using BiSON data to within  $2\sigma$ , and this period implies a cycle-averaged latitude of around  $8^\circ$ . This agrees with the conclusions drawn from our inferences of the BiSON data, that the RM source is linked to ARs.

The line-width suggests a RM lifetime of  $175 \pm 13$  days, which is in the region of  $\sim 25$  weeks or half a year. This lifetime is inconsistent with that measured using the BiSON data, however. The lifetime measured in the BiSON power spectrum is around 50% larger than that measured with the WSO data. A possible explanation for this could be the resolution differences of the two instruments, or more likely it is a by-product of the different regions within the photosphere they probe, as discussed above. These limits are still consistent however with the lifetime of large, strong ARs (Schrijver & Harvey, 1994; van Driel-Gesztelyi & Green, 2015).

As with the BiSON observations, the investigation of the WSO SMMF also indicates the origin of the SMMF is linked to ARs and MFCs that are long-lived on the solar disk and exist in active latitudes.

## 1.6 Discussion

### 1.6.1 Asymmetry in the Power Spectrum

We have shown that the BiSON and WSO SMMF power spectra are best modelled with asymmetric Lorentzian profiles. In this section, we investigate the cause of this asymmetry.

An initial hypothesis on the origin of the asymmetry was the migration of active regions towards the equator with the progression of the solar cycle. This is illustrated clearly by the asymmetry in the rotation frequencies of sources at latitudes sampled from a Kernel Density Estimate (KDE) of the SSN, in combination with models for the differential rotation (Snodgrass, 1983) and equatorial migration (Li et al., 2001a), shown in Figure 1.11. The migration of ARs towards the equator has an asymmetry which is skewed towards lower frequencies, in accordance with the asymmetry of the Lorentzian peaks in the BiSON and WSO power spectra. If the total power spectrum is the sum of the power spectra for each contributing source, which have central frequencies following the distribution shown in Figure 1.11, then we may expect to see this same asymmetry manifested in the power spectrum.

To investigate migration as a source of the asymmetry, we used artificial data which were created to simulate the differential rotation and migration of active regions during the solar cycle. The methodology involved with generating the simulated data is discussed in Appendix A, and here we discuss the outcomes.

Three separate models for the migration of ARs towards the equator were used in the simulations and they are shown in Figure 1.12a. The quadratic model was taken from Li et al. (2001a), which represents a ‘typical’ migration of ARs, and the linear and exponential models were parametrised to provided opposite extremes for

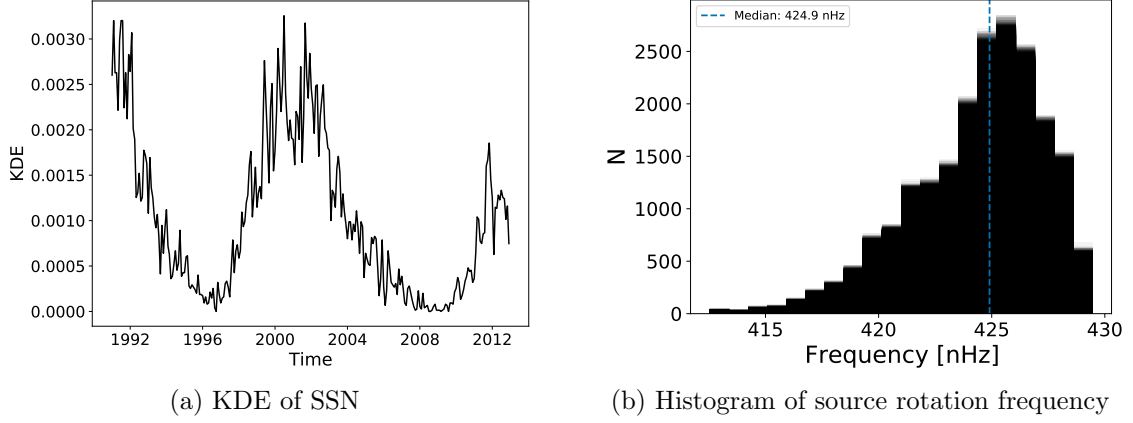


Figure 1.11: (a) Shows the KDE of the monthly averaged sunspot number used to draw samples of source seed times; (b) distribution of the rotation frequency of sources sampled from the KDE, after using the model for the migration and differential rotation.

a slower and faster migration towards the equator, respectively. The aim of this was to investigate whether varying the migration rate affected the asymmetry. Each migration model is given in equation (1.25), (1.26), and (1.27), where  $t$  is the time since the start of the cycle, in years.

$$\lambda_q = 0.0893t^2 - 2.8t + 27.24 \quad (1.25)$$

$$\lambda_l = -1.84t + 27.24 \quad (1.26)$$

$$\lambda_e = 20.24e^{-t/2} + 7 \quad (1.27)$$

In Figure 1.12 we also note that for each model of the migration, we saw a different median rotation frequency in the distribution, which was lower for the slower migration, and higher for the faster migration. This was expected, due to the differential rotation, but it shows that the measured central rotation frequency of the SMMF power spectrum was sensitive to the migration and tells us something about the source. This also suggested that the RM component on the SMMF power spectrum was consistent with a faster migration model.

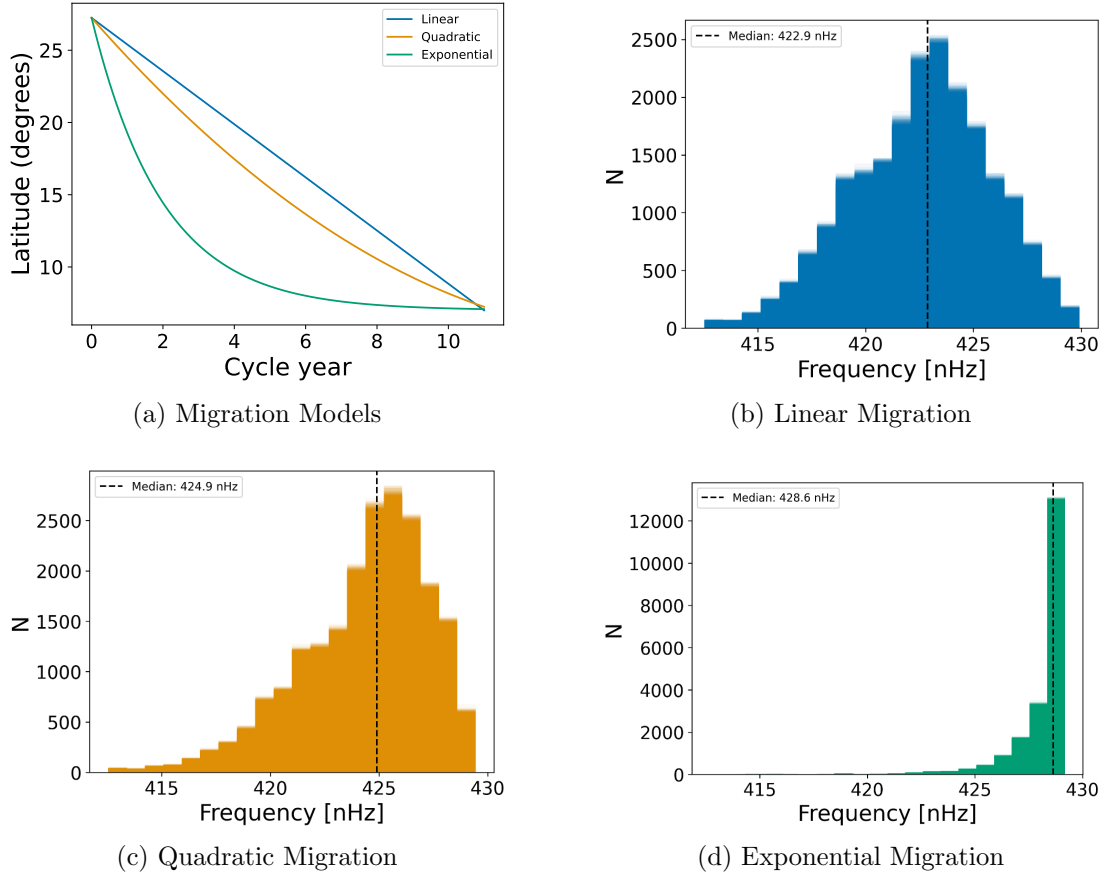


Figure 1.12: (a) Shows the latitudinal migration model as a function of time for each model; (b)-(d) shows the distribution of the rotation frequencies of sources sampled from the KDE for linear, quadratic, and exponential migration models, respectively.

The simulations were run with 15 different configurations which used the three migration models combined with five models for the source transits across the visible disk (see Appendix A: cosine model, sign change model, and combinations of the cosine and sign change models in ratios of 5:95, 10:90, and 20:80). In each case, 250 simulations were performed in order to produce a limit spectrum. Each limit spectrum was modelled with a series of Lorentzian peaks sharing a global asymmetry parameter, and the resultant asymmetry values are shown in Figure 1.13.

It was immediately clear that the choice of migration model had no significant effect on the asymmetry of the Lorentzian peaks, hence we are able to rule out AR migration as the origin of the asymmetry observed. A possible reason for this explanation is that it was not correct to suggest that the total power spectrum

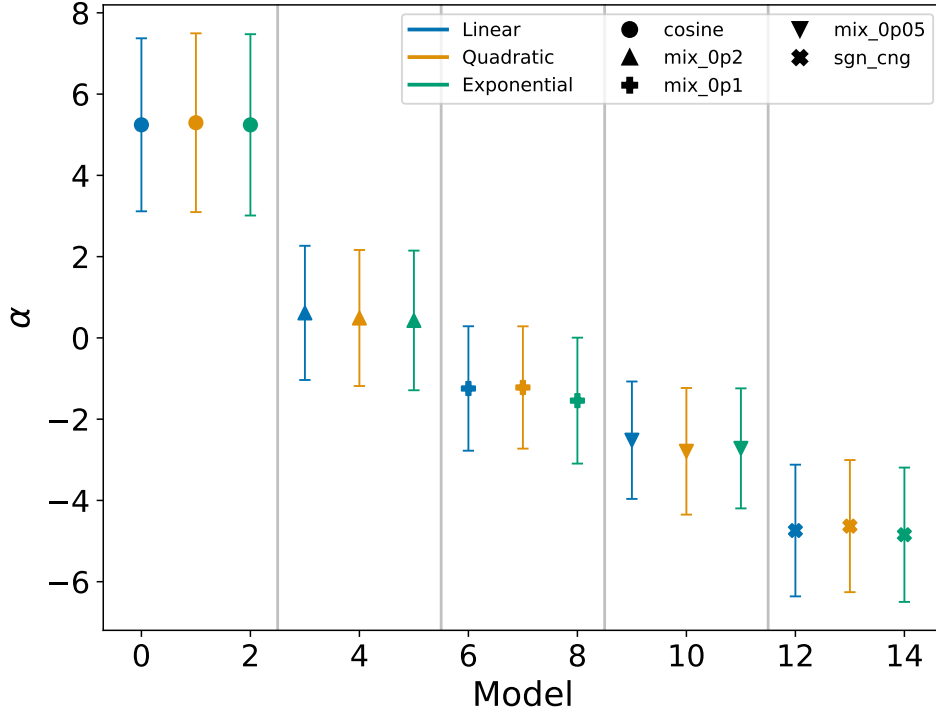


Figure 1.13: The median value of the fitted global asymmetry parameter for several simulations of artificial data. The colour represents the migration model used: linear:blue; quadratic:orange; exponential: green. The marker represents the source model used: cosine:circle; sign change:cross; combinations of the cosine and sign change models in ratios of 5:95:downwards triangle; 10:90:plus; 20:80:upwards triangle.

is the sum of power spectra for each individual source, because this neglects the interference between sources in the time domain. However, this figure did show an obvious difference between the way the different models of the sources have asymmetry manifested in their spectra.

This links to a still-open debate in helioseismology, on the source of asymmetry of the modes in the power spectra, and the asymmetry reversal between the observations in intensity and Doppler velocity. Asymmetry is regularly observed in  $p$  modes of oscillation in helioseismic data and we observe a difference in the sign of the asymmetry term which is negative for Doppler velocity observations (i.e. more power in the low-frequency wing of the mode) and positive for measurements made in intensity (i.e. more power in the high-frequency wing of the mode) (Duvall et al., 1993; Chaplin & Appourchaux, 1999; Howe et al., 2015; Basu & Chaplin, 2017).

There are believed to be two main causes of asymmetry in acoustic modes:

1. The spatially localised nature of the excitation source of acoustic modes in the near-surface layers of the outer convection zone and the interference between multiple waves that have accumulated a phase difference since their emission. This source of asymmetry is believed to dominate in Doppler velocity observations.
2. The correlation between the convective granulation (i.e. correlated noise) and the signal from the modes themselves, or the correlation between the excitations of one mode to another. This source of asymmetry is believed to dominate in intensity observations due to the lower signal-to-noise ratio.

We believe that some combination of phase difference between sources, and noise arising from the randomness of the simulations is responsible for the asymmetry difference observed between the cosine and sign change models, as they replicate the difference in the ways we observe the ARs, either by intensity (cosine model) or Doppler velocity (sign change model).

In the case of the SMMF observations, we believe the asymmetry is explained by the first of the above explanations. Active magnetic regions are typically localised in the near-surface layers of the Sun and we see clear interference between different regions of magnetic flux which form the observed more prominent active regions, which we believe contribute strongly to the SMMF. The interference between small regions of flux will have accumulated a phase difference and therefore could contribute to the observed asymmetry.

On the second point, the SMMF is measured by the Zeeman splitting of an emission line due to the magnetic field, which is inherently measuring the Doppler shift, i.e. ‘velocity’. There is no bleed through of  $p$  mode power in the spectrum, and we have shown that there is no red-noise-like signal or stochastic background with a short timescale resembling granulation in the power spectrum; therefore, it

is unlikely that we see a strong correlated noise contribution which would produce the asymmetry in the SMMF RM component peaks.

### 1.6.2 Testing the Effects of Differential Rotation and Active Region Migration

We know the rotation period of ARs varies throughout the solar cycle as a result of solar differential rotation and latitudinal migration. As we have inferred that the RM component of the SMMF is likely linked to ARs and MFCs, we may therefore assume that the RM component is also sensitive to these effects. Here we analyse the effect of migration and differential rotation on our ability to make inferences on the lifetime of the RM component.

Several studies have modelled the the solar differential rotation, and its variation with latitude and radius of the Sun (see Beck (2000) and Howe (2009) for an in depth review of the literature on solar differential rotation). Magnetic features have been shown to be sensitive to rotation deeper than the photosphere; therefore, in general, magnetic features can be seen to rotate with a shorter period than the surface plasma (Howe, 2009).

Chaplin et al. (2008) analysed the effects of differential rotation on the shape of asteroseismic low- $l$   $p$  modes of oscillation, and showed that the consequence of differential rotation is to broaden the observed line-width of a mode peak. The authors provide a model of the resultant profile of a  $p$  mode whose frequency is shifted in time to be a time-average of several instantaneous Lorentzian profiles with central frequency  $\nu(t)$ , given by equation (1.28). The angled brackets indicate an average over time.  $H$  and  $\Gamma$  are the mode height (maximum power spectral density) and line-width, respectively. The full period of observation is given by  $T$ .

$$\langle P(\nu) \rangle = \frac{1}{T} \int_0^T H \left( 1 + \left( \frac{\nu - \nu(t)}{\Gamma/2} \right)^2 \right)^{-1} dt \quad (1.28)$$

Chaplin et al. (2008) also show that by assuming a simple, linear variation of the

unperturbed frequency,  $\nu_0$ , from the start to the end of the time-series by a total frequency shift  $\Delta\nu$  (see equation (1.29)),

$$\nu(t) = \nu_0 + \Delta\nu \frac{t}{T} \quad (1.29)$$

the resultant profile of a  $p$  mode can analytically be modelled by equation (1.30):

$$\langle P(\nu) \rangle = \frac{H}{2\epsilon} \arctan \left( \frac{2\epsilon}{1 - \epsilon^2 + X^2} \right) \quad (1.30)$$

where  $\epsilon$  and  $X$  are defined in equation 1.31 and equation 1.32.

$$\epsilon = \frac{\Delta\nu}{\Gamma} \quad (1.31)$$

$$X = \frac{\nu - [\nu_0 + (\Delta\nu/2)]}{\Gamma/2} \quad (1.32)$$

As the mode line-widths are broadened by this effect, we evaluate whether our ability to resolve the true line-width of the RM component, and hence its lifetime, is affected. To evaluate this we computed the broadened profiles given by both equation (1.28) and equation (1.30), and fit the model for a single Lorentzian peak, to determine whether the line-width is recovered.

In the first instance, we computed the broadened peak using equation (1.28). Over the duration of the observations, we computed the daily instantaneous profile,  $P(\nu(t))$ . The time-averaged profile,  $\langle P(\nu) \rangle$ , is a weighted average of each instantaneous profile, where the weights are given by the squared, daily-averaged SMMF, in order to allow a larger broadening contribution at times when the SMMF amplitude is large.

In the second instance, we computed the broadened peak using equation (1.30). Over the duration of the observations the daily frequency shift is computed,  $\Delta\nu$ . The time-averaged shift,  $\Delta\nu$ , is a weighted average, where again the weightings are



given by the squared, daily-averaged SMMF.

To determine the shift in the rotation rate with migration, we used the model of the solar differential rotation as traced by magnetic features ( $\Omega_m$ ) given by equation (1.33), where  $\mu = \cos \theta$  and  $\theta$  is the co-latitude (Snodgrass, 1983; Brown et al., 1989). Finally, the time-dependence on the latitude of the active regions used the best-fitting quadratic model by Li et al. (2001b).

$$\frac{\Omega_m}{2\pi} = 462 - 74\mu^2 - 53\mu^4 \text{ nHz} \quad (1.33)$$

In both instances, the broadened peak was modelled as a single Lorentzian peak using equation (1.13), with a width equivalent to that which was inferred from modelling the BiSON power spectrum. We use `emcee` (Foreman-Mackey et al., 2013) to explore the posterior parameter space with priors similar to the fit to the full power spectrum.

Over the entire duration of the SMMF observations, the time-averaged profile was calculated, using equation (1.28), and this is shown in Fig. 1.14a. The broadened mode used the input parameters outlined in Table 1.2, however, with the background parameter set to zero. For the input, we show the posterior width that resulted from the model to the BiSON, which is shrunk due to the convolution process, rather than the more realistic width of  $\sim 15\%$

By eye, the broadened profile does not appear to have a significantly larger line-width. The fit to the time-averaged broadened peak produced a line-width of  $0.0315 \pm 0.0041 \mu\text{Hz}$ . The line-width of the broadened peak under this method is rather unchanged from that of the true peak, and both line-widths are within uncertainties of each other.

The time-averaged frequency shift due to differential rotation was calculated, much in the same way as equation (1.28), to be  $\Delta\nu = 0.01285 \mu\text{Hz}$ . This shift was used to generate the broadened profile using equation (1.30). The broadened mode distribution also used the input parameters outlined in Table 1.2, however, with the

Table 1.4: Input line-width and the median posterior values of the Lorentzian model each simulation. Numbers in brackets denote uncertainties on the last 2 digits, and all uncertainties correspond to the 68% credible intervals either side of the median.

Input Value	Weighted Fit	Analytic Fit	Unit
$0.0316^{(+07)}_{(-07)}$	$0.0315 \pm 0.0041$	$0.0315 \pm 0.0041$	$\mu\text{Hz}$

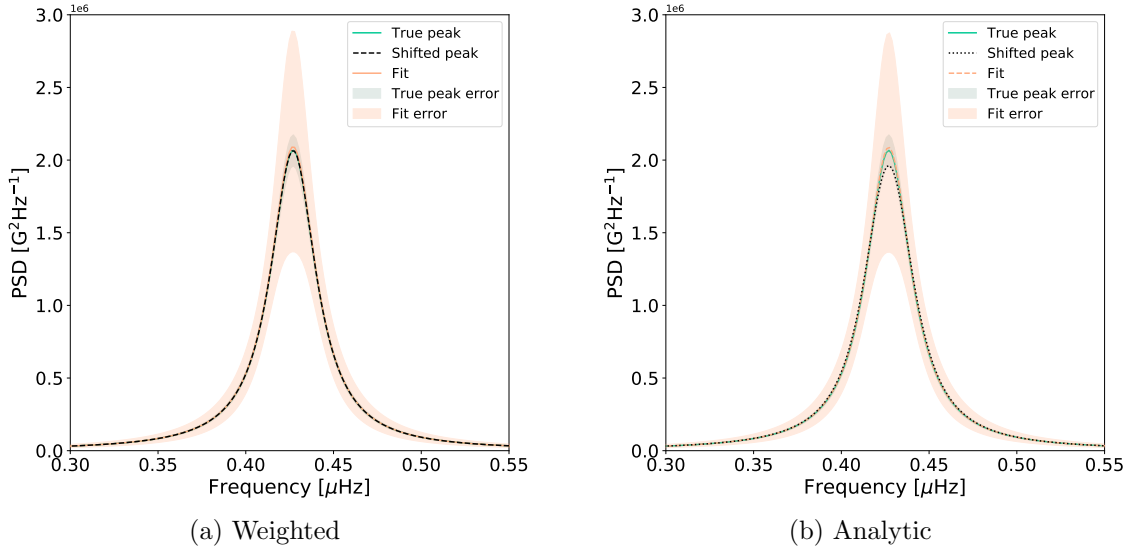


Figure 1.14: (a) Shows the Lorentzian distribution peak before and after the time-averaged broadening, and the fit to the broadened peak. (b) Shows the peak distribution before and after the analytical broadening, and the fit to the broadened peak. In both plots the broadened peaks have been shifted by the relevant frequency to overlay them on top of the true  $\nu_0$  for comparison.

background parameter set to zero.

Similarly to the numerically broadened peak, by eye, the analytically broadened profile does not appear to have a significantly larger line-width and the resultant median posterior values of the fitted Lorentzian profile are shown in Table 1.4. The line-width of the analytically broadened peak from the fit is  $0.0315 \pm 0.0041 \mu\text{Hz}$ , which is within the uncertainties of the line-width of the input peak.

These results show that both numerically and analytically, the mode broadening effect of differential rotation and latitudinal migration does not affect our ability to resolve the line-width of the peaks. Both broadening methods applied have been shown to have a negligible effect on the measured line-width. This result provides confidence that the line-width in Table 1.2 is the true line-width of the RM peaks,

thus providing the correct lifetime for RM component, unaffected by migration and differential rotation.

### **1.6.3 Further Morphology of the SMMF using SDO/HMI Data**

In Chapter 2 we acquired SDO/HMI full-disk magnetograms, using the `SunPy` python module (Barnes et al., 2020), to support our investigations into Rossby waves.

Owing to having the SDO/HMI magnetograms, which provided the capability to separately analyse the Northern and Southern Hemispheres' MMF contribution to the SMMF during the rising phase of Cycle 24 in 2011 and during solar maximum in 2014, we also investigated whether there were hemispheric differences in the data, which resulted from the opposite polarities at high latitudes and towards the poles. This served as a further analysis into other timescales which may exist in the SMMF. In particular, we investigated if the SMMF exhibited an anti-correlation between the two hemispheres due to the oppositely polarised field near the polar regions, such as that which is found in synoptic charts, on a time-scale of the solar cycle.

To support this investigation, we acquired the synoptic charts from SDO/HMI. It was possible to also average the signal over the Northern and Southern Hemispheres of the synoptic charts, as well as the full solar surface, thus providing a comparison to the hemispheric MMF and the full disk SMMF.

To compare the magnetogram data to the synoptic charts, we smoothed the separately averaged Northern and Southern Hemispheres' MMF and the full-disk SMMF signals using a box-car filter with a window width of a Carrington period, i.e.  $\sim 27$  days. The resultant time series was plotted along with the hemispheric mean of the synoptics charts from SDO/HMI. Figure 1.15 shows the resultant smoothed hemispheric MMF and full-disk SMMF along with the average of the synoptic charts.

We can see from Figure 1.15 that there does exist a longer timescale in the hemi-

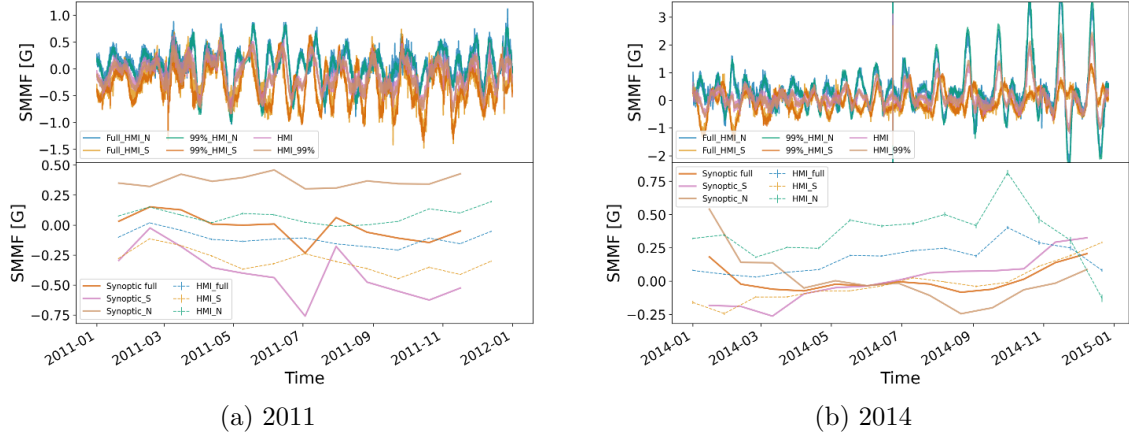


Figure 1.15: Investigations of timescales in the SDO/HMI magnetograms over 2011 and 2014. Both plots show in the top panel, the hemispheric MMF and full-disk SMMF from the magnetograms. The lower panel of each plot displays a comparison between the hemispheric and full-disk mean of the synoptic charts, compared to the box-car smoothed MMF from the magnetograms. N: Northern hemisphere; S: Southern hemisphere. Full HMI: considers the full solar disk; 99 HMI: considers only the inner 99% of the solar disk, by radius.

spheric MMF when we average out the effects of the RM component. This is visible from the reversal of the field polarity in 2014. This longer timescale component resembles the average of the synoptic charts, and shows the secular variation which is contributed from the solar dipole at high latitudes. This timescale is the solar activity period, and it can be seen particularly in Figure 1.15b whereby the dipole magnetic field undergoes a reversal at around solar maximum, with the onset of the rush of magnetic field to the poles.

Interestingly, the field reversal was located during different epochs when comparing the synoptic chart data to the visible disk, hemispheric MMF data, and was delayed in the hemispheric MMF by around 7 Carrington rotations.

Naturally, when the full-disk averaged SMMF was smoothed using the box-bar filter, the RM component was averaged out, resulting in a near-flat line. This was however expected as it was the average of the opposite hemispheres, and is consistent with the synoptic charts.

## 1.7 Conclusion

Observations of the SMMF have been computed from the Zeeman split D1 line of Potassium at  $\sim 770$  nm, as measured by the Sutherland node of BiSON. The observations covered a period from 1992 – 2012 with a cadence of 40 seconds. A frequency-domain analysis of the SMMF was performed; the short cadence and long baseline of observations gave a fine frequency resolution in the power spectrum up to a high Nyquist frequency, allowing us to probe the elements that underpin the observed SMMF.

The duty cycle for the 40-second cadence observations was very low, hence the effect of the low fill on the power spectrum of the SMMF was investigated to help inform how to best model the full power spectrum. We highlighted that although there appeared to exist a red-noise-like, stochastic background component in the power spectrum, this was a feature originating from power aliasing due to the low duty cycle of the observations.

In the power spectrum, there was a strong peak at a frequency corresponding to the solar rotation, denoted the RM signal/component. It was also demonstrated that the low duty cycle aliased the power of the prominent peak due to the solar rotation to higher frequencies, which provided several copies of this peak at higher frequencies.

Using a model comprising of a series of Lorentzian peaks to model the RM signal, a Harvey function to account for lower frequency drifts, and shot-noise limit, which was convolved with the Fourier transform of the window function to account for the low duty cycle artefacts, we modelled the full power spectrum and measured the properties of the RM signal.

It was demonstrated that the convolution process affected the total power in the model, thus careful treatment was taken to ensure Parseval’s theorem was obeyed. In addition, it was shown that the width of the posterior distributions for the pa-

rameters had shrunk, as a result of the convolution process, because the likelihood evaluation did not fully take into account the correlated noise on the power spectrum due to the convolution. We could not account for this, but it was highlighted and a comparison between a model with and without convolution was used to help provide an estimate of the true uncertainties on the parameters.

A comparative study was conducted on the WSO data over the same observational epoch and the modelled power spectrum provide results that were in agreement with those measured in the BiSON power spectrum.

To further investigate the SMMF and our ability to infer the properties of the source, we used simulations to analyse the effects of differential rotation and AR migrations on our ability to measure the line-width, and the origin of the asymmetric peak shape.

Finally, a short investigation into the SMMF as measured by SDO/HMI was conducted. Smoothing the data over the solar rotation period for both Northern and Southern hemispheres, separately, uncovered that the hemispheres display a longer variation, in accordance with the solar activity cycle, similar to that of the full-disk synoptic maps.

We leave the reader with the following points:

1. We have shown that there does not exist a short time-scale component in the SMMF, and its emergence was due to the low duty cycle of the BiSON observations.
2. By modelling the peak of the RM signal as an asymmetric Lorentzian profile, we find that the peak has a central frequency of  $0.4278 \pm 0.0001 \mu\text{Hz}$ . This measurement of the central frequency allowed us to infer the sidereal period of the RM signal to be  $25.19 \pm 0.01$  days (note: this uncertainty is underestimated from the convolution shrinking the posterior; the estimated, representative  $1\sigma$  posterior width is approx.  $\pm 0.1$  days). This rotation suggests a magnetic

feature, cycle-averaged latitude of  $\sim 11^\circ$ , thus linking the source to active bands of latitude on the Sun.

3. The lifetime of the source of the RM component was inferred from the line-width of the Lorentzian peaks to be  $116.5 \pm 2.6$  days (note: this uncertainty is underestimated from the convolution shrinking the posterior; the estimated, representative  $1\sigma$  posterior width is approx.  $\pm 15$  days).
4. As a comparison, the power spectrum of the SMMF measured by WSO was also modelled and the line-width and central frequency of the RM component were measured. The results were generally consistent with those from the BiSON data, and the conclusions inferred are in accordance.
5. The measured properties of the RM component of the SMMF are consistent with ARs. The literature advises that sunspots are not the origin of the SMMF, so we suggest that ARs and MFCs are the source of the dominant, rotation signal in the SMMF, that are long-lived on the solar disk and exist in active latitudes.
6. We have shown that our ability to determine the line-width and hence lifetime of the RM modes was unaffected by AR migration and differential rotation.
7. Through simulating artificial SMMF data, we explored the source of the asymmetry in the model. We believe the asymmetry is a result of the phase interference between localised, near-surface regions of MFCs.
8. Finally, a short investigation into the hemispheric contributions to the SMMF, using data from SDO/HMI, showed there is a longer-term variation which underpins the SMMF, in accordance with the activity cycle and polar field reversals.

At the time of writing, only two more of the BiSON nodes were actively measuring the SMMF (Las Campanas and Narrabri), and their measurements of the

SMMF are not as stable as those measured by the Sutherland node. Sutherland has not been measuring the SMMF since 2013, however. More work is required to fix the issues with measuring the SMMF using BiSON, such that the frequency resolution can be further increased with a longer baseline, allowing for more accurate inferences on the SMMF morphology.

With more time on the project, it would also be useful to develop a technique similar to Kutsenko et al. (2017) and Bose & Nagaraju (2018), which allows the SMMF to be dissected into regions and features on the disk.



## 2 Rossby Modes in the Solar Mean Magnetic Field

### 2.1 Introduction

Rossby waves, as first derived by Rossby & Collaborators (1939), have recently been discovered in the Sun through observations of near-surface flows by the Solar Dynamic Observatory Helioseismic and Magnetic Imager (SDO/HMI) (Löptien et al., 2018; Liang et al., 2019).

Rossby waves, or  $r$  modes, are toroidal modes of oscillation of a rotating, fluid body for which the dominant restoring force against the pressure gradients is the Coriolis force (Lanza et al., 2019; Hathaway & Upton, 2020). Rossby waves are associated with an undulation of a flow resulting in a pattern of radial vorticity of alternating sign. They are understood to form in the high atmosphere on Earth, heavily influencing global weather. For the Sun we observe that Rossby waves propagate in the retrograde direction, in the Carrington reference frame.

Recently, Löptien et al. (2018) provided an unambiguous detection of sectoral solar  $r$  modes by tracking the horizontal flows of granules in the solar photosphere during a 6-year period, using observations by SDO/HMI. Following this study Liang et al. (2019) confirmed the detection of solar  $r$  modes with time-distance helioseismology to measure deeper, subsurface flows in the meridional direction along the solar equator using both Solar and Heliospheric Observatory Michelson Doppler Im-

ager (SOHO/MDI) and SDO/HMI data, covering 21 years. In addition, Hanasoge & Mandal (2019) were also able to show the detection of solar  $r$  modes using a normal-mode coupling technique on 2 years of SDO/HMI data. In both of the observation conducted by Löptien et al. (2018) and Liang et al. (2019), the average lifetime of the  $r$  modes were on the order of several months, and as long as a over a year for specific modes.

By monitoring the proper motions of solar supergranules using a local correlation tracking method Hathaway & Upton (2020) also report observing low latitude Rossby waves in full-disk Doppler images obtained by SDO/HMI, extending the measurements of Rossby waves to greater depths in the solar atmosphere, by an order of magnitude. The  $r$  modes observed using the supergranules have lifetimes which are only slightly longer than the Carrington rotation period, hence in slight disagreement with Löptien et al. (2018) and Liang et al. (2019), which Hathaway & Upton (2020) claim may be due the waves getting in and out of phase with each other as the low wave number waves propagate faster than the higher wave number waves. As these observations are at low latitudes, it is possible that they are linked to active magnetic regions and hence could be manifested in other sources of magnetic data.

Here we present the possible detection of the to-date unobserved, lowest frequency sectoral  $r$  mode using 21 years of Birmingham Solar Oscillations Network (BiSON) observations of the Line Of Sight (LOS) Solar Mean Magnetic Field (SMMF) (for details on the SMMF and BiSON, see Chaplin et al. (2003) and references within).

In an earlier study of the SMMF, the power spectrum of the BiSON observations was modelled using a combination of Lorentzian peaks and a convolution with the window function to account for the effect of gaps in the data. The full spectrum and the fit are shown in Figure 2.1.

We can divide through by the model, to achieve the residual spectrum, in which

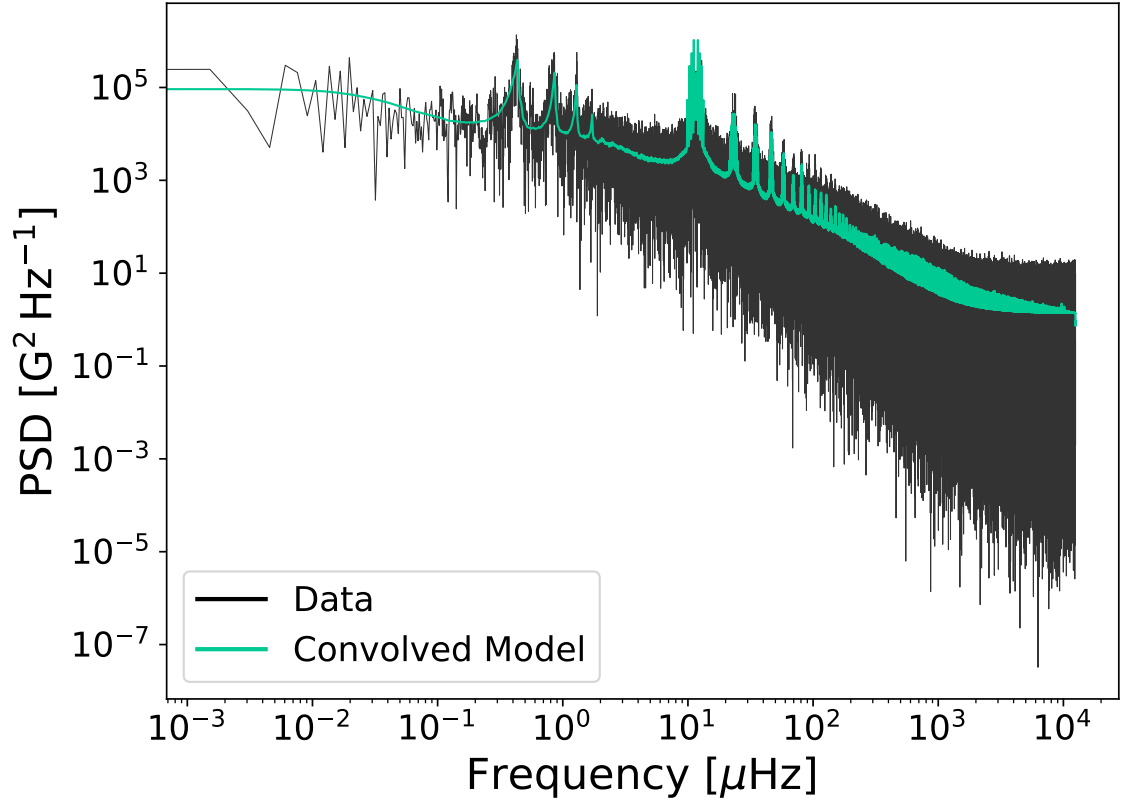


Figure 2.1: Full, modelled power spectrum of the BiSON SMMF on logarithmic axes. The data is displayed in black and the convolved model using asymmetric Lorentzian peaks is shown in green.

we have investigated and potentially found the signature of  $r$  modes. We find that although there exists a promising narrow-band region of significant power in the BiSON residuals spectrum, which could be the  $l = m = 2$  mode, the  $r$  mode does not exist in other sources of SMMF data, hence the observed peak is more likely explained as being a source of prominent noise in the BiSON observations.

## 2.2 Aims

In this chapter the residual power spectrum of the BiSON SMMF, after removing a model for the dominant signal, was investigated in order to search for the existence of  $r$  modes. Within the residual spectrum we test for the existence of  $r$  modes and where they appear to exist, a Lorentzian model is fit to the peak to understand the properties of the source.

Further analysis is provided using simulated data to better understand how an annual modulation of the  $r$  mode observations would affect their frequencies. In addition, SDO/HMI data are investigated to support the argument that  $r$  modes are not split in the power spectrum and instead we should observe the central mode frequency and lower amplitude side bands.

## 2.3 Theory

The detailed theory of the effect of  $r$  modes on observational data was re-visited recently by Lanza et al. (2019) in light of the solar observations, in an effort to determine the effect of the  $r$  modes on radial velocity detections of exoplanets.

Under the assumption of a slow, uniformly rotating sphere (with angular velocity,  $\Omega$ , where  $\Omega^2 \ll GMR^{-3}$ ), the frequencies of global  $r$  modes in the Carrington rotating frame is well approximated by equation (2.1), where  $l > 0$  is the angular degree and  $m$  is the azimuthal order (Löptien et al., 2018; Lanza et al., 2019).

$$\nu_{carr} = -\frac{2m\Omega}{l(l+1)} \quad (2.1)$$

In an inertial frame the observed  $r$  mode frequencies will be (Lanza et al., 2019):

$$\nu_{in}(l, m) \approx m\Omega - \frac{2m\Omega}{l(l+1)} = m\Omega \left(1 - \frac{2}{l(l+1)}\right) \quad (2.2)$$

where  $\Omega$  is the mean sidereal rotation rate, and  $l$  and  $m$  are the angular and azimuthal degree, respectively. Sectoral Rossby waves are obtained by setting  $l = m$  in this equation. A consequence is that they propagate with a retrograde phase velocity as  $\nu/m = -2\Omega/[m(m+1)] < 0$ .

An Earth-based observer, orbiting the sun, shall expect to observe frequencies adjusted by the orbital frequency,  $\nu_{\oplus} \approx 31.7\text{nHz}$ , given by equation (2.3).

$$\nu_{obs}(l, m) = \nu_{in}(l, m) - m\nu_{\oplus} \quad (2.3)$$

In addition, due to the tilt of the ecliptic with respect to the solar equatorial plane (the solar  $B_0$  angle), the visibility of the modes will vary on a timescale of 1 year, meaning we expect to actually observe split peaks at frequencies of  $\nu_{\text{obs}}(l, m) \pm \nu_{\oplus}$  (Lanza et al., 2019)).

Based on this theory, we can compare the observed sectoral  $r$  modes with those predicted. These frequencies are summarised in Table 2.1.

Table 2.1: Predicted<sup>+</sup> and observed<sup>o</sup>  $r$  mode frequencies for combinations of  $l$  and  $m$ . Predicted frequencies and conversions of observations to different frames of reference use equation (2.1), equation (2.2), and equation (2.3), with  $\Omega = 453.1$  nHz. The predicted splitting for the  $B_0$  angle variation is also provided. The key for the source column is: LPT for Löptien et al. (2018), LNG for Liang et al. (2019), and LZA for Lanza et al. (2019).

Frequency	Source	$l = m = 2$	$l = m = 3$	$l = m = 4$	$l = m = 5$
$\nu_{\text{carr}} [nHz]$	LPT <sup>o</sup>	–	-259	-194	-157
	LNG <sup>o</sup>	–	-253	-198	-156
	LZA <sup>+</sup>	-302.1	-226.6	-181.2	-151.0
$\nu_{\text{in}} [nHz]$	LPT	–	1100	1618	2109
	LNG	–	1106	1614	2110
	LZA	604.1	1132.8	1631.2	2114.5
$\nu_{\text{obs}} [nHz]$	LPT	–	1005.2	1491.7	1950.1
	LNG	–	1011.2	1487.7	1951.1
	LZA	540.8	1037.7	1504.4	1956.0
$\nu_{\text{obs}} + \nu_{\oplus} [nHz]$	LPT	–	1036.9	1523.3	1981.8
	LNG	–	1042.9	1519.3	1982.8
	LZA	572.4	1069.4	1536.1	1987.7
$\nu_{\text{obs}} - \nu_{\oplus} [nHz]$	LPT	–	973.6	1460.0	1918.4
	LNG	–	979.6	1456.0	1919.4
	LZA	509.1	1006.0	1472.7	1924.3

## 2.4 Methodology

### 2.4.1 Testing the Residual Spectrum

In order to investigate the presence of Rossby wave modes in the power spectrum of the BiSON SMMF, statistical significance tests were employed using a false-alarm approach, to test the probability of finding prominent narrow-band power in the residual spectrum.

We assume negative exponential statistics (i.e.  $\chi^2$  2-degrees of freedom distribution), and that the bins in the power spectrum are uncorrelated (an assumption which may be incorrect due to the low fill-factor of the BiSON SMMF data). Then we can find the false alarm probability, or probability to observe power in a given frequency bin,  $\nu$ , that is greater than or equal to a given threshold.

The probability to observe power in a given frequency bin,  $\nu$ , that is greater than or equal to  $P(\nu)$  is:

$$p[P(\nu)] = \frac{1}{P_{lim}(\nu)} \exp\left(-\frac{P(\nu)}{P_{lim}(\nu)}\right) \text{ or; } p[P(\nu)] = \frac{1}{\langle P(\nu) \rangle} \exp\left(-\frac{P(\nu)}{\langle P(\nu) \rangle}\right), \quad (2.4)$$

where  $P_{lim}(\nu)$  is the limit spectrum or  $\langle P(\nu) \rangle$  is a well-fitting model/estimate to the spectrum. Considering a relative power approach (i.e. considering the power relative to the mean level or model of the Power Spectral Density (PSD)), equation (2.4) may be written more concisely as:

$$p(s_\nu) = e^{(-s_\nu)}, \quad (2.5)$$

where,

$$s_\nu = P(\nu)/\langle P(\nu) \rangle, \quad (2.6)$$

and  $\langle P(\nu) \rangle$  is reduced to 1 when we compare the power relative to the power spectrum residuals.

In reality, we use the  $\chi^2$  cumulative distribution function to compute the probability of power, which is given by equation (2.7), where  $k$  is the number of degrees of freedom,  $\gamma(s, t)$  is the lower incomplete gamma function and  $P(s, t)$  is the regularized gamma function.

$$F(x; k) = \frac{\gamma(\frac{k}{2}, \frac{x}{2})}{\Gamma(\frac{k}{2})} = P\left(\frac{k}{2}, \frac{x}{2}\right) \quad (2.7)$$

Using these expressions, we can rewrite the equation for  $P(s_\nu)$  as given by equation (2.8). This allows us to compute the probability of statistically significant peaks in the residuals for re-binned data.

$$p(s_\nu) = 1 - F(2s_\nu; k) = 1 - P\left(\frac{k}{2}, s_\nu\right) \quad (2.8)$$

The probability that a bin has power at or above the level  $s_\nu$  is therefore given by equation (2.5), or more generally by equation (2.8), hence the probability that we fail to find a bin with power at or above the level  $s_\nu$  is  $1 - p(s_\nu)$ ; thus the probability of failing to find a bin with power at or above  $s_\nu$  in  $N$ -bins in the spectrum is  $[1 - p(s_\nu)]^N$ . Therefore the probability to find at least one bin with power at or above  $s_\nu$  in  $N$ -bins in the spectrum is:

$$p_N = 1 - [1 - p(s_\nu)]^N \quad (2.9)$$

where a low value for  $p_N$  indicates that the spike in power in that bin is unlikely to be a statistical fluctuation, and therefore is considered a statistically significant spike.

This can be generalised using the cumulative binomial distribution. The probability of finding at least  $r$  spike in  $N$ -bins at or above the relative power level  $s_\nu$  is given by equation (2.10), which is equal to equation(2.9) when  $r = 1$ .

$$p[r; p(s_\nu), N] = 1 - Pr(X < s_\nu) = \sum_{r=r}^N \binom{N}{r} p(s_\nu)^r [1 - p(s_\nu)]^{N-r} \quad (2.10)$$

By applying equation (2.10) to the residuals of in the power spectrum, we can test whether there are any significant peaks in the residual power spectrum. Again,

a low value for  $p[r; p(s_\nu), N]$  indicates that the power in that bin is unlikely to be a statistical fluctuation.

## 2.4.2 Modelling $r$ mode Profiles

In the location of any suspected  $r$  modes in the residual spectrum, we can model the profile of the peak by using a Lorentzian distribution, using the form expressed by equation (2.11), where  $A$  is the amplitude of the signal,  $\Gamma$  is the line-width of the distribution, and  $\nu_0$  is the central frequency of the distribution. This follows the methodology adopted by Löptien et al. (2018) and Liang et al. (2019).

$$P(\nu) = \frac{2A^2/(\pi\Gamma)}{1 + (2(\nu - \nu_0)/\Gamma)^2} \quad (2.11)$$

Modelling was performed using the `pymc3` No U-Turn Sampler (NUTS) extension to a Hamiltonian Monte Carlo (HMC) sampling algorithm (Salvatier et al., 2016).

## 2.5 Results

### 2.5.1 Testing the Residual Spectrum

The residual spectrum is shown in Figure 2.2, with the removed model and locations of  $r$  mode frequencies predicted by Lanza et al. (2019) over-plotted.

It is clear from Figure 2.2 that there appears to be a resolved peak of narrow-band power in both the location of the  $l = m = 2$   $r$  mode and perhaps also the upper  $B_0$ -variation-modulated  $l = m = 3$   $r$  mode.

The statistics tests were performed on the residual spectrum for various re-binning factors,  $n$ . The plots summarising the statistics tests are shown in Fig. 2.3 for re-binning factors of  $n = 1, 2, 5$ , and  $10$ .

These tests suggest that the feature around  $0.5 \mu\text{Hz}$  may be a signal related to  $r$  modes, as its location is roughly correct for the  $l = m = 2$  mode consistently has a low False Alarm (FA) probability. The other low FA probability features tend to



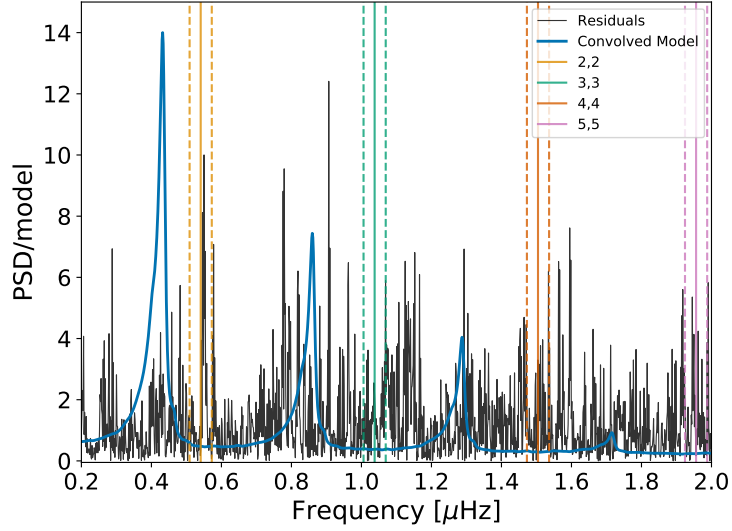


Figure 2.2: Residual power spectrum of the BiSON SMMF. Over plotted in the green curve is the model of the main SMMF signal. Also over plotted as vertical solid lines are the expected locations of the 4 lowest-frequency sectoral  $r$  modes and the dashed lines, the locations of the  $B_0$  variation frequency splitting. Dashed lines represent  $\pm 31.7$  nHz (i.e. representing the frequencies of splitting due to the variation in the  $B_0$  angle.)

be associated with the residuals from the main harmonics of the SMMF signal, and are the result of a slight failing of the main model of the power spectrum.

In particular in Figure 2.3b, there is compelling evidence to suggest that this peak is significant. In order to solidify this conjecture, we aimed to fit a model to the residuals around this peak in order to confirm whether the properties of the peak resembled those suggested by Löptien et al. (2018), Liang et al. (2019), and Lanza et al. (2019).

### 2.5.2 Modelling $r$ mode Profiles

Using the model for the Lorentzian peak (eq. 2.11), we modelled the residual spectrum around the location of the potential  $l = m = 2$  mode. The results of the fit are given in Table 2.2 and the fit to the residuals is shown in Figure 2.4.

The median of the posterior distribution for the width parameter suggests an e-folding lifetime ( $1/(\pi\Gamma)$ ) of around 650 days ( $\sim 1.8$  years), which follows the order magnitude of the lifetime suggested by low- $m$  Rossby modes. The lowest  $r$  mode observed,  $l = m = 3$ , was shown to exhibit a lifetime of over a year ( $\sim 1.4$  years) by

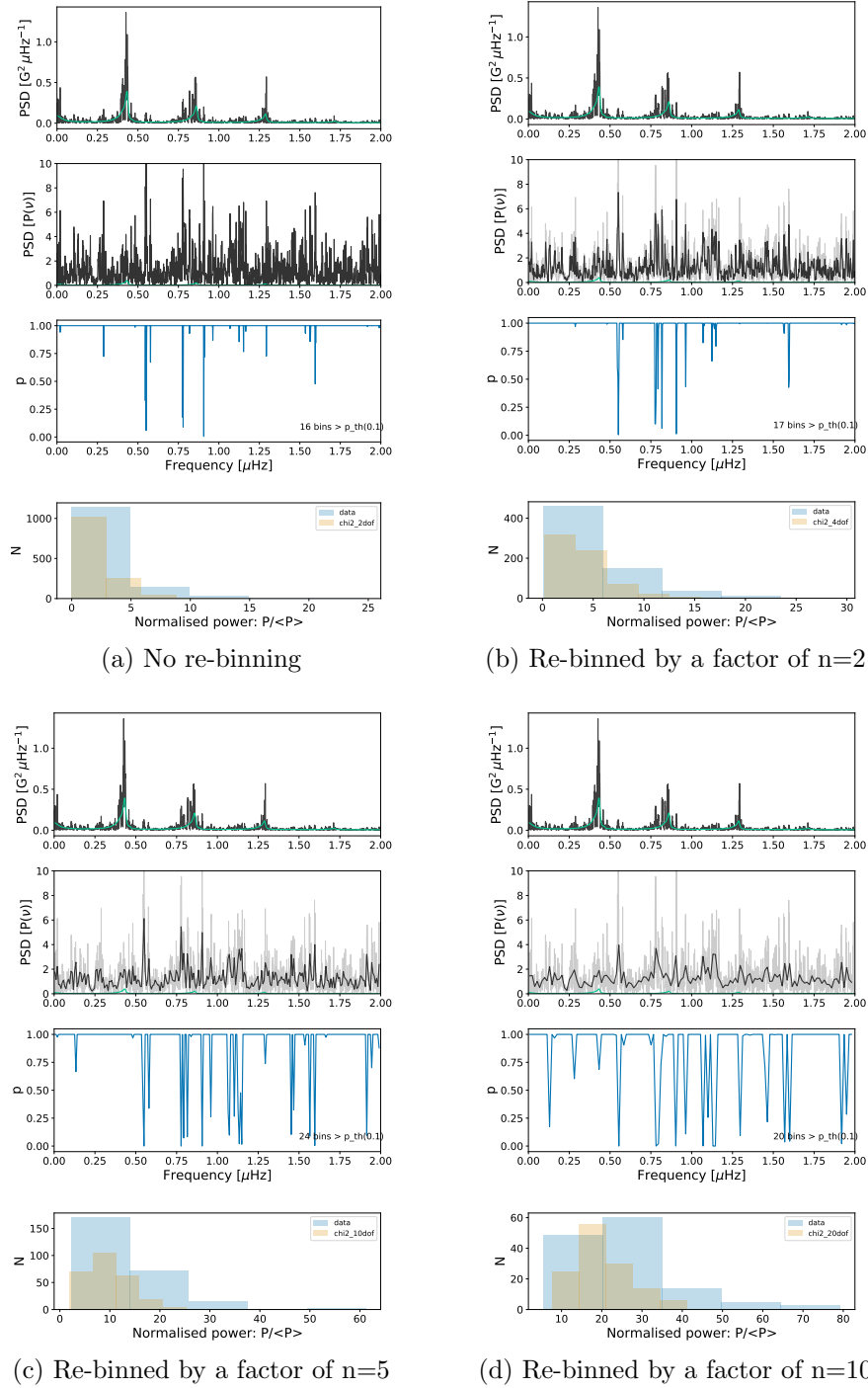


Figure 2.3: Realisations of the statistics tests on the BiSON data for different re-binning factors ( $n$ ). The panels of each sub figure are: (top) the full PSD and fit, (second panel) the full and re-binned residuals, (third panel) the probability of statistical noise in each bin, (bottom) distribution of the residuals compared to a  $\chi^2$   $2n$ -DOF.

Liang et al. (2019). The  $l = m = 4$  were observed by both Löptien et al. (2018) and Liang et al. (2019) to have a lifetime of  $\sim 0.6$  years and  $\sim 0.3$  years, respectively.

Table 2.2: Median posterior values of the Lorentzian model for the  $r$  mode peak in the BiSON SMMF PSD residuals. Numbers in brackets denote uncertainties on the last 2 digits, and all uncertainties correspond to the 68% credible intervals either side of the median.

Parameter	Value	Unit
$\nu_0$	$0.5500^{(+16)}_{(-16)}$	$\mu\text{Hz}$
$\Gamma$	$0.0058^{(+45)}_{(-28)}$	$\mu\text{Hz}$
$A$	$0.261^{+0.063}_{-0.049}$	—
$bgnd$	$1.00 \pm 0.16$	—

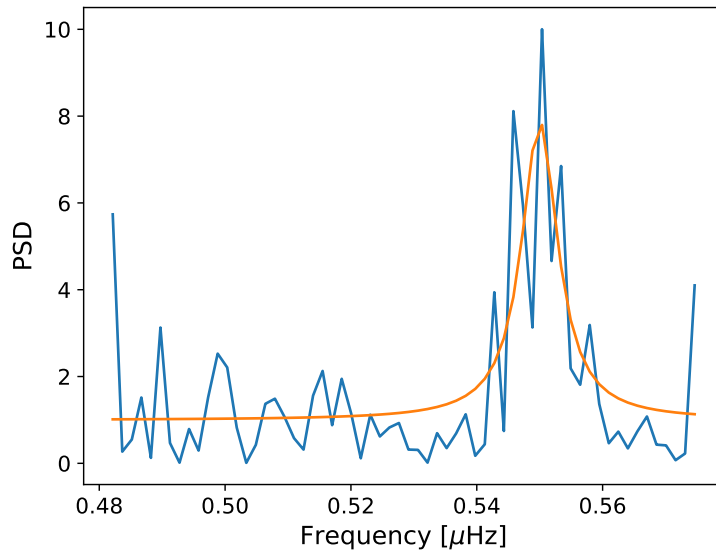


Figure 2.4: Model fit to the  $r$  mode in the BiSON PSD residuals using the median from the parameter posterior distributions.

There seems to be a slight increasing trend in the mode lifetimes observed by Löptien et al. (2018) and Liang et al. (2019) of longer lifetimes for lower  $m$ , therefore the long lifetime found here for the  $l = m = 2$  mode is entirely reasonable and in-line with current observations.

The model of the mode in the residuals spectrum has a magnetic amplitude of  $\sim 30$  mG, which equates to a radial velocity amplitude of  $\sim 8.7 \text{ cm}^{-1}$ . Lanza et al. (2019) state that the maximum RV amplitude of the  $l = m = 2$  mode is  $\sim 24.5 \text{ cm}^{-1}$ , meaning our observed peak is around a third of the maximum RV amplitude one might have expected to observe. This is however an upper limit given by Lanza et al. (2019), and therefore the lower amplitude in the model should not be concerning.

In particular, however, we can see that the background is  $\sim 1$ , which is expected for such a fit to residual PSD data. Due to the accuracy of the background, the agreement between the central frequency of the fit to the  $l = m = 2$  mode, the agreement in the order of magnitude of the e-folding lifetime, and the amplitude of the mode residing below the upper limit suggested by Lanza et al. (2019), we believe there is strong evidence to suggest that this peak, which has shown to be significant through the false-alarm statistics tests, is the  $l = m = 2$  sectoral  $r$  mode, observed in the BiSON SMMF data.

## 2.6 Discussion

Despite the compelling results presented in the previous section there remained an open question on the way the Rossby waves would manifest themselves in the power spectrum. The BiSON power spectrum was also compared to the power spectra of the Wilcox Solar Observatory (WSO) SMMF and the SDO/HMI SMMF to cross-reference the finding.

### 2.6.1 Manifestation of Rossby Waves in the Power Spectrum

It was suggested by Lanza et al. (2019) that the mode should be split into two frequencies due to the annual variation of the  $B_0$  angle, but the observed peak in the BiSON spectrum is located at approximately the location of the central frequency; therefore the observation is not split due to this modulation. We needed to determine if this was physically observable.

Figure 2.5 shows a schematic diagram of the flow of a  $l = 2 = m$  sectoral  $r$  mode. One can clearly see from the more visible purple region of the schematic, the Southern Hemisphere flow is oriented out of the page, whereas the Northern Hemisphere flow is oriented into the page. Due to the  $B_0$  modulation, a varying of the sign of the flow would be observed over this region, i.e the velocity of the flow.

In the more red-green regions the schematic, the flow is more transverse, hence this would contribute less to the effect of the  $B_0$  modulation.

We needed to therefore understand whether the SMMF observations have a hemispheric dependence that would lead to a change sign in the observations due to the  $B_0$  variation. In addition, this raised the question of how the mode was affected in the power spectrum by the  $B_0$  modulation; either split into separate peaks as suggested by Lanza et al. (2019) or instead was it possible that we could have a situation where the mode at the central frequency remained?

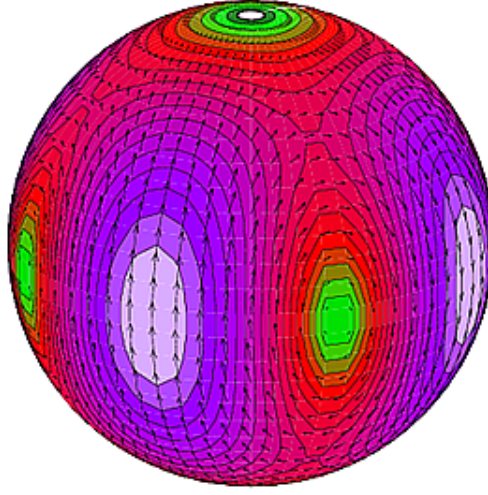


Figure 2.5: Mode displacement schematic for an  $l = m = 2$   $r$  mode (Strohmayer & Mahmoodifar, 2014)

To investigate the splitting of the mode, a simple model was produced whereby a sinusoidal function (with a period of  $\sim 25$  days) was modulated by either a cosine or rectified cosine function (with a period of 1 year). In the former, using the cosine modulation, this represents observing the sign of the flow varying with the  $B_0$  modulation. Conversely in the latter simulation, this instead represents a variation of the amplitude, and it does not change the sign. Figure 2.6 shows the time series of the two cases to more clearly show their difference. The power spectrum of each case was then computed and these are shown in Figure 2.7 to demonstrate the differences between the modes produced.

One can clearly see the difference in the power spectrum produced in each of the

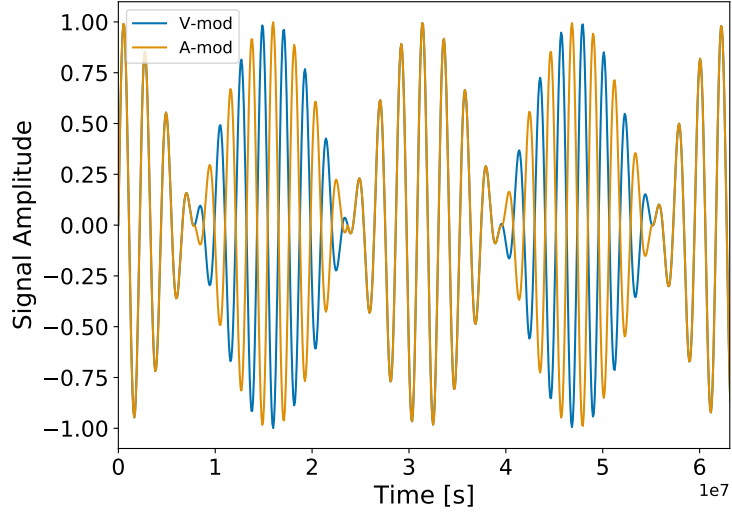


Figure 2.6: Time series of the velocity and amplitude modulation toy model simulations. The blue curve shows the velocity modulation, i.e. modulating using a cosine with period of 1 year, whereas the orange curve shows the amplitude modulation, i.e. modulating using a rectified cosine with period 1 year.

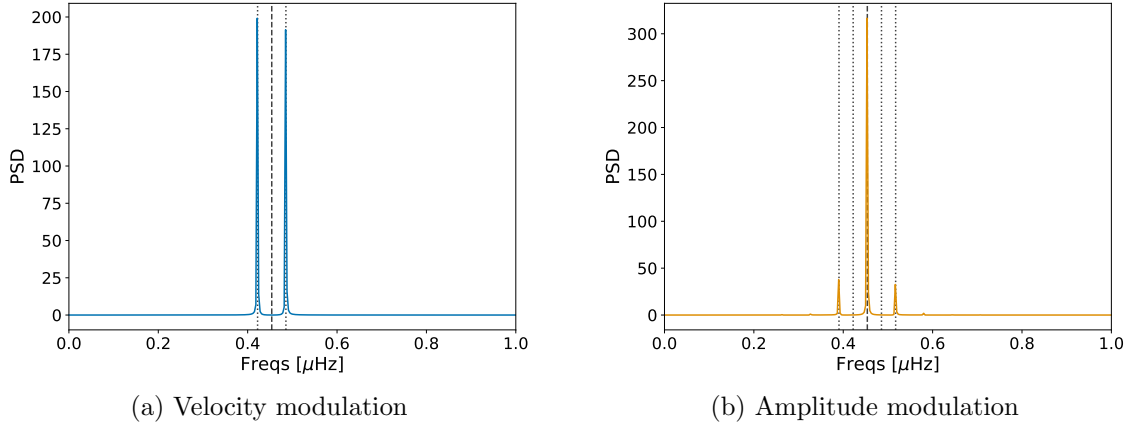


Figure 2.7: Power spectra for the two modulation methods, showing the difference in the way the modulation has changed the frequency of the observed mode.

cases. In the velocity modulation case, we see a splitting of the oscillation mode into two peaks split around the expected mode frequency by  $\pm\nu_{\oplus}$ . There exists no more power at the central mode frequency in this case and is in agreement with the scenario suggested by Lanza et al. (2019). In the amplitude modulation case, we see a production of sidebands at  $\pm 2\nu_{\oplus}$  however the expected mode frequency remains in this scenario and has a significantly higher peak height, a ratio of 90:10 in favour of the central peak.

We have shown that it is possible to retain the central frequency of the  $r$  mode in the power spectrum if the  $B_0$  modulates the amplitude of the observations and not the sign. With this known, it was then necessary to understand whether the two hemispheres of the Sun contribute signals that are more analogous with the velocity modulation or amplitude modulation. In the former, velocity modulation, we would expect to see a persistent anti-correlation between the two hemispheres. In the latter, amplitude modulation, we would expect to see the signals from each hemisphere that are correlated, which track each other and which can be both positive or negative.

We investigated how the two hemispheres of the Sun contribute to the SMMF through analysis of SDO/HMI data. To do this, we acquired 720s-cadence magnetograms from SDO/HMI using the `SunPy` python module (Barnes et al., 2020) for the rising phase of solar cycle 24 during 2011, and for the maximum of cycle 24 during 2014. It was possible to separately average the Northern and Southern Hemispheres' contributions to the total, disk-averaged SMMF. The plot of this data is shown in Figure 2.8.

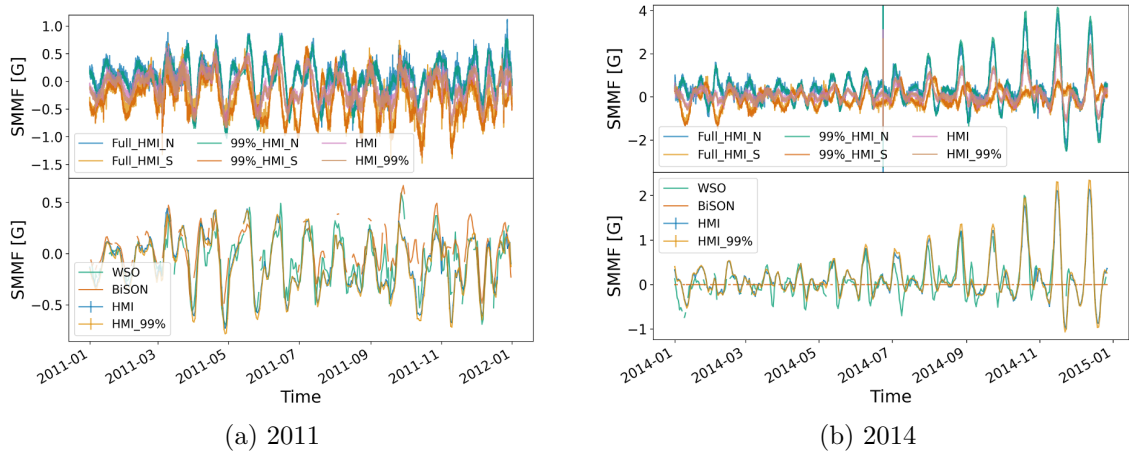


Figure 2.8: SDO/HMI SMMF split into hemispheres and compared to other SMMF sources during (a) 2011, and (b) 2014. The top panel in each figure shows the north (N), south (S), and total disk-averaged mean magnetic field, for both the full solar disk and from pixels within 99% of solar radius. The bottom panels show a comparison between the SMMF, as observed BiSON, WSO, and SDO/HMI (full disk and the 99% disk).

The hemispheric contributions to the total, disk-averaged, SMMF can be seen in Figure 2.8 to track each other during 2011, and both become positive or negative. By contrast, when observing the hemispheric contributions to the full SMMF in 2014, we see that there are frequent periods of strong anti-correlation between the Northern and Southern Hemispheres. There are also several periods in 2014 whereby the two hemispheres are correlated. This plot aids in our understanding of how the  $r$  modes would be manifested in the power spectrum due to the variation of the  $B_0$  angle.

As there are periods of both strong correlation and strong anti-correlation between the two hemispheres, this is a good indication that the  $r$  mode signal would result in a central frequency with sidebands due to the correlation between North and South. But due to the existence of periods of anti-correlation between North and South, we also expect there to be some degree of frequency splitting in the power spectrum, but this is dependent on how prevalent the anti-correlation is over the entire solar cycle; in these short epochs however, we expect this to be minimal. It is therefore possible to conclude that we are confident we are observing the  $l = 2 = m$   $r$  mode.

As a further point, we see that there is both strong correlation and strong anti-correlation between the Northern and Southern Hemispheres, however this does not necessarily mean that the  $r$  mode signal would directly manifest itself in the same way. We can see from Figure 2.5 that if the  $r$  mode observations are constrained to active latitude bands, closer to the equator, then the effects of the  $B_0$  are less prominent.

### 2.6.2 Rossby Modes in Other Sources of SMMF Data

To further investigate whether the observation of the  $l = 2 = m$   $r$  mode is real, a comparison was made between the power spectrum of the BiSON observations of the SMMF and those from WSO and SDO/HMI, to determine whether the suspected



$r$  mode is visible. In the case of the WSO, the power spectrum was computed over the same observing epoch as the BiSON data (i.e. from 1992 – 2013); however SDO was not launched until 2010, so for HMI the power spectrum was computed on data from 2010 – 2020, hence at approximately half the frequency resolution of WSO and BiSON.

Figure 2.9 shows the comparison of the WSO and SDO/HMI power spectra reflected around the x-axis against the BiSON power spectrum. In both cases we see a good agreement between the different sets of data on the location of the rotational mode in the SMMF, but there does not appear to be a visible  $r$  mode candidate in the WSO or the SDO/HMI data.

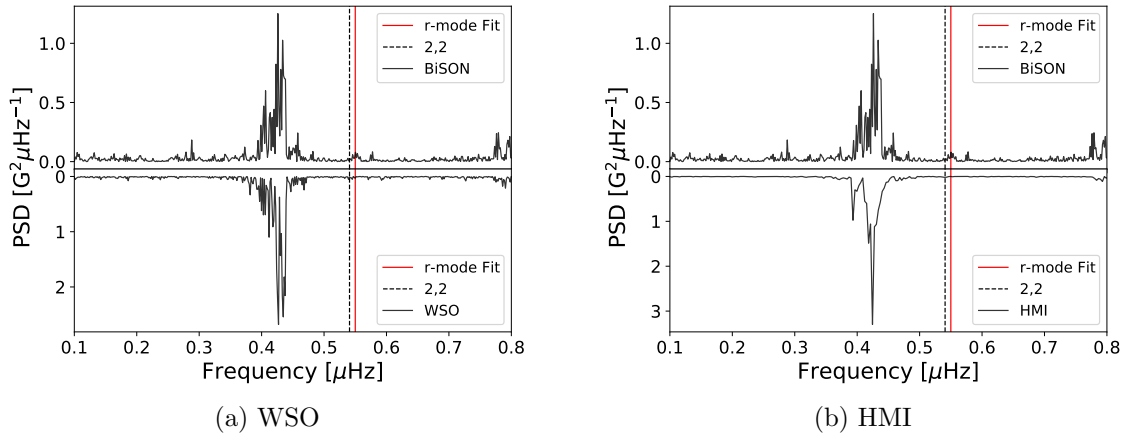


Figure 2.9: Comparison of the power spectra for BiSON, WSO, and SDO/HMI. In both figures, the top panel shows the BiSON PSD and the bottom panel shows either the WSO or HMI PSD. The dashed, black line shows the location of the theoretical  $l = 2 = m$   $r$  mode frequency, and the red, solid line shows the location of the peak fit in the BiSON PSD residuals.

This provides concerning evidence that we may not, in fact, have observed the  $l = 2 = m$   $r$  mode in the BiSON power spectrum, and perhaps instead we have a persistent noise source in the BiSON SMMF.

However convincing the results are, suggesting that we have observed the  $l = 2 = m$   $r$  mode in the BiSON power spectrum, we cannot ignore that it is not present in two other sources of SMMF observations, of which one of these telescopes is responsible for providing the recent observations of  $r$  modes documented in the

literature. Owing to this, we cannot conclude that we have observed the  $l = 2 = m$   $r$  mode in the BiSON power spectrum. Searching for  $r$  modes in the power spectra of the SMMF observations should be revisited in a few years, or say a solar cycle's time, when the frequency resolution in each spectra has increased significantly, to provide a more insightful follow-up study.

## 2.7 Conclusion

After removing the model for the BiSON SMMF power spectrum we investigated the residual spectrum to search for the existence of Rossby wave modes ( $r$  modes). Using a false-alarm approach we estimated the probability of finding narrow-band power. We identified the existence of a statistically significant peak which was near the  $l = 2 = m$   $r$  mode frequency calculated by Lanza et al. (2019).

Using a Lorentzian model for the peak, following the description of  $r$  mode given by Löptien et al. (2018) and Liang et al. (2019), we identified the properties of the peak, and compared them to the existing literature. The work by Lanza et al. (2019) stated that the  $l = 2 = m$   $r$  mode should be observed at a frequency of  $\sim 540.8$  nHz, with a maximum amplitude of  $24.5 \text{ cm}^{-1}$ . The recent observations of low-degree sectoral  $r$  modes by Löptien et al. (2018) and Liang et al. (2019) claimed the line-width of the mode would be on the order of around 10 nHz, due to the e-folding lifetime of the mode being on the order of a year.

To further interrogate the inferences on the  $r$  mode in the BiSON SMMF power spectrum, we use simple simulations to determine how the  $r$  mode may manifest itself in the power spectrum, using the modulation of the signal due to the variation in the  $B_0$  angle. Furthermore, SDO/HMI hemispheric data were employed to verify these results.

As a final check, we compared the power spectrum of the SMMF observations from BiSON to those from WSO and SDO/HMI. There was no clear signature of the  $l = 2 = m$   $r$  mode in either of the other power spectra, which rules our observation of

an  $r$  mode in the BiSON SMMF very suspicious, especially as the recent observations of sectoral Rossby waves in the Sun have all used SDO/HMI data.

We leave the reader with the following points:

1. Through a series of false-alarm probability statistical tests, we have shown that there exists a statistically significant peak in the BiSON SMMF residuals spectrum which is located near the theoretical frequency of the  $l = 2 = m$   $r$  mode.
2. By modelling the peak as a Lorentzian profile we find that the peak has a central frequency of  $550 \pm 16$  nHz (i.e. located  $\sim 9.2$  nHz from the theoretical frequency), a line-width of  $5.8^{+4.5}_{-2.8}$  nHz, and an amplitude of  $\sim 30$  mG. This profile is within the upper limit for the amplitude of the  $l = 2 = m$   $r$  mode and the life time implied by the line-width is on the order of 1–2 years, which is in agreement with the observations by Löptien et al. (2018) and Liang et al. (2019).
3. Through the analysis of simulated data and hemispheric observations of the SMMF, we have shown that we should expect to see a prominent mode at the theoretical frequency, and not a split mode due to the effect of the  $B_0$  variation, which supported the findings of the  $r$  mode.
4. By comparing the power spectrum of the SMMF observed by BiSON, to those of WSO and SDO/HMI, we have shown that the  $r$  mode peak is not manifested in either the WSO or SDO/HMI spectra, therefore ruling it highly unlikely that the observed peak in the BiSON spectrum is the  $l = 2 = m$   $r$  mode.

As we collect more observations of the SMMF using BiSON, the frequency resolution of the power spectrum increases. An obvious next step in this work is to collect more observations of the SMMF with BiSON, to further investigate if this suspected mode remains resolved, or whether it diminishes into the noise.

# A Simulations of the Artificial SMMF

## A.1 Model

The artificial data used in the simulations of the Solar Mean Magnetic Field (SMMF) were created using 2 very simplistic models, either separately or in combination, which were physically motivated by sunspots and Active Regions (ARs) on the solar surface (van Driel-Gesztelyi & Green, 2015):

1. **Cosine:** in this model a source was simulated as a single region which ingresses visible disk from one limb, traverses across the disk, before egressing the other limb (see Fig. A.1a). The physical motivation for this would be a single, concentrated source of imbalanced magnetic flux. This method induces no sign change of the simulated source; it remains the same polarity always. This was simulated as a rectified sinusoidal signal, with a 50% duty cycle (i.e. it is only visible during times on near-side of the disk).
2. **Sign change:** in this model a source was simulated as 2 regions of opposite polarity, such as sunspot pairs or a Bipolar Magnetic Region (BMR). The leading region contributes more at the start of the transit during ingress, and the trailing source contributes more at the end of the transit during egress; hence at the middle of the transit we assume there is a sign change in the overall signal, see Fig. A.1b. This was simulated as a rectified sinusoidal signal, and was multiplied by a cosinusoidal signal of the same period to provide the

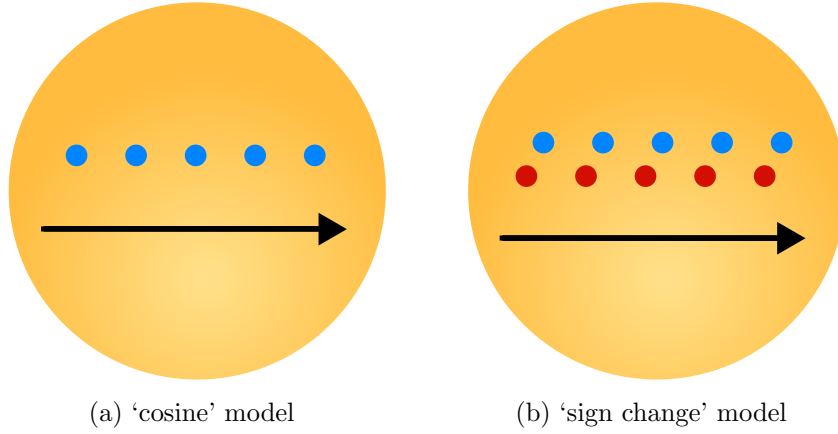


Figure A.1: Schematic representations of the two models of the artificial SMMF. (a) shows the cosine model with a single source of constant polarity transiting the visible disk. (b) shows the sign change model whereby there are 2 regions of opposite polarity transiting the disk, and their contribution to the SMMF changes during the transit.

projection of the pair of regions. This operation results in a rectified sinusoidal signal with half the period.

There were several variables that allowed us to change the physics of the simulations. These were:

- $N$ : Number of sources
- $t_0$ : Start time of source appearance
- $A$ : Amplitude of sources
- $\lambda$ : Latitude of sources
- $\tau$ : Decay time of sources
- $\phi$ : Additional phase of sources

Using these variables, the mathematical forms of the two model types for a single source are expressed by equation (A.1) and equation (A.2). In these equations  $t' = t - t_0$ ,  $\Pi_{P/2}(t)$  is a window function to define the transit period of the simulated source on the visible side of the solar disk,  $\text{III}_P$  is a Dirac comb of repetition period,

$P$ , and  $\Pi_T(t)$  is a window function defining the total observation period. The time series of a single modelled source for each model is shown in Figure A.1.

$$B_{\text{cosine}}(t) = \left[ A e^{-t'/\tau} \left( \cos \left( \frac{2\pi}{P} t' + \phi \right) \Pi_{P/2}(t) \right) * \text{III}_P \right] \times \Pi_T(t) \quad (\text{A.1})$$

$$B_{\text{sign-change}}(t) = \left[ A e^{-t'/\tau} \left( \cos \left( \frac{2\pi}{P} t' + \phi \right) \sin \left( \frac{2\pi}{P} t' + \phi \right) \Pi_{P/2}(t) \right) * \text{III}_P \right] \times \Pi_T(t) \quad (\text{A.2})$$

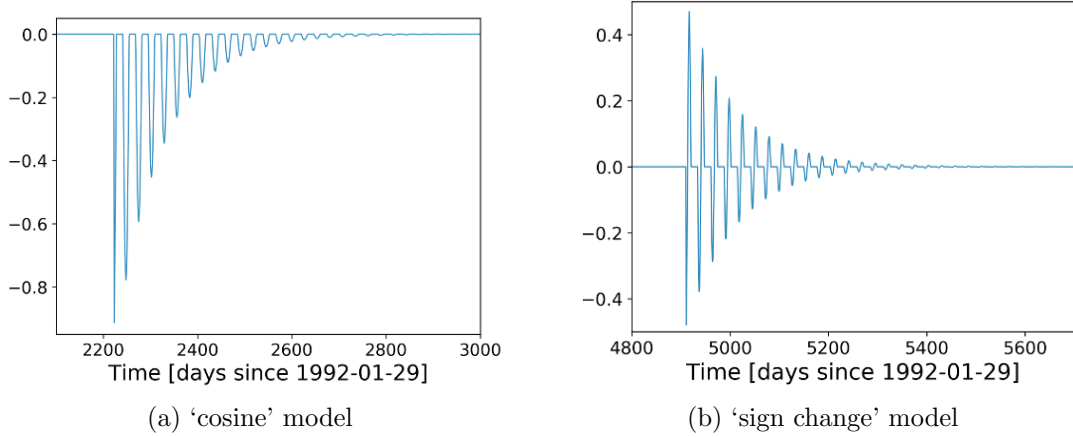


Figure A.2: A single realisation of (a) the cosine model, and (b) the sign change model.

## A.2 Configuration of the Simulations

A flowchart describing the steps in the simulations is shown in Figure A.3. The simulations require the user to select the number of sources to be modelled. Using this information, the user selects whether to draw  $N$  seed/start times ( $t_0$ ) from either a Kernel Density Estimate (KDE) of the Sun Spot Number (SSN), or from a uniform distribution between the start and end times. The former will give an output which is more physical, but the latter is useful for testing.

From the generated seed times, latitudes are computed using a model for the migration of spots during the Solar Cycle (Li et al., 2001b), and the differential

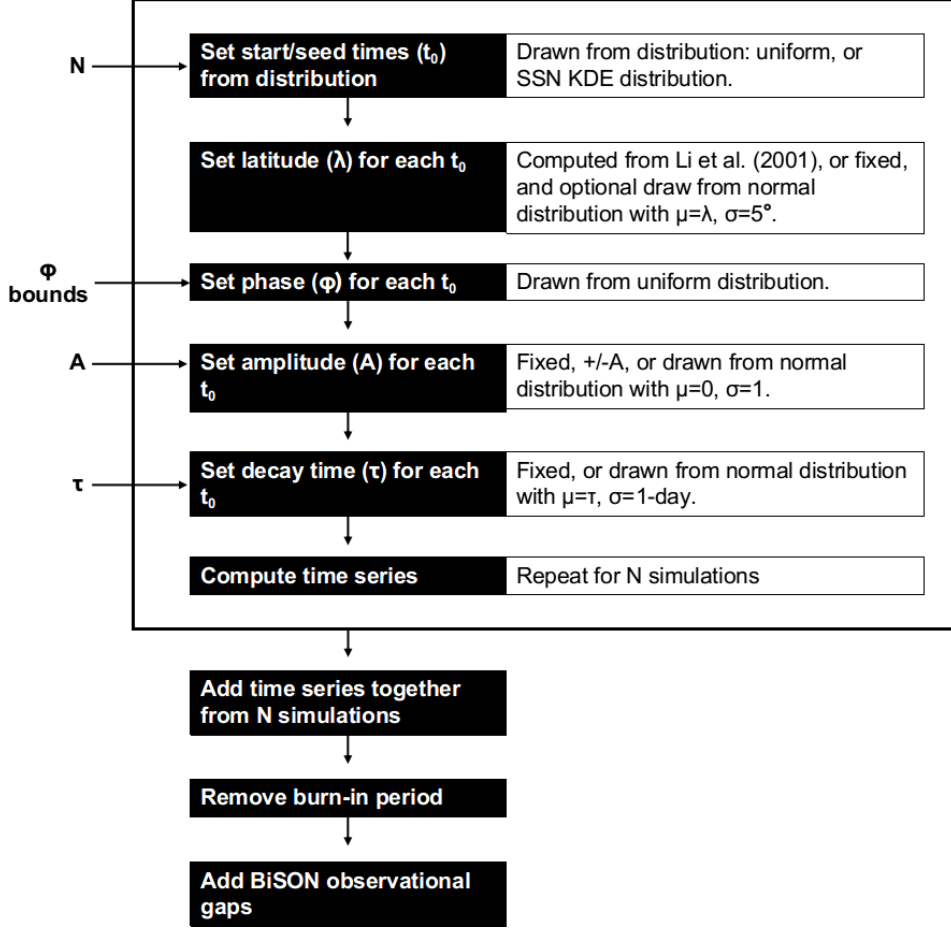


Figure A.3: Flowchart showing the step-by-step processes in the generation of the artificial SMMF time series data.

rotation frequency at that latitude is taken from a model of the solar differential rotation (Snodgrass, 1983).

Values are then assigned for the phase, amplitude, and decay time of each source (the user can set these parameters, or it is also possible to randomly draw them from a distribution). Each individual source is simulated according to equation (A.1) or equation (A.2). Following the simulation of  $N$  sources, the full time-series is computed by adding all  $N$  source contributions together. Finally, a burn-in period is removed, which allows the artificial SMMF to settle prior to the start of ‘observations’, and then we can inject gaps into the artificial time series which are concurrent with the gaps in the Birmingham Solar Oscillations Network (BiSON) observations.

The aim of creating artificial data was to produce a representative power spec-

trum to that of the BiSON SMMF. We assumed that the sources of the SMMF are ARs and Magnetic Flux Concentration (MFC)s, therefore we aimed to produce a time series that physically represented these sources, i.e. comparable to the sunspot number. To do this we produced an average number of sources on the visible disk during close to the sunspot number. At solar maximum during cycle 23, the number of daily spots on the disk is around 150 – 200.

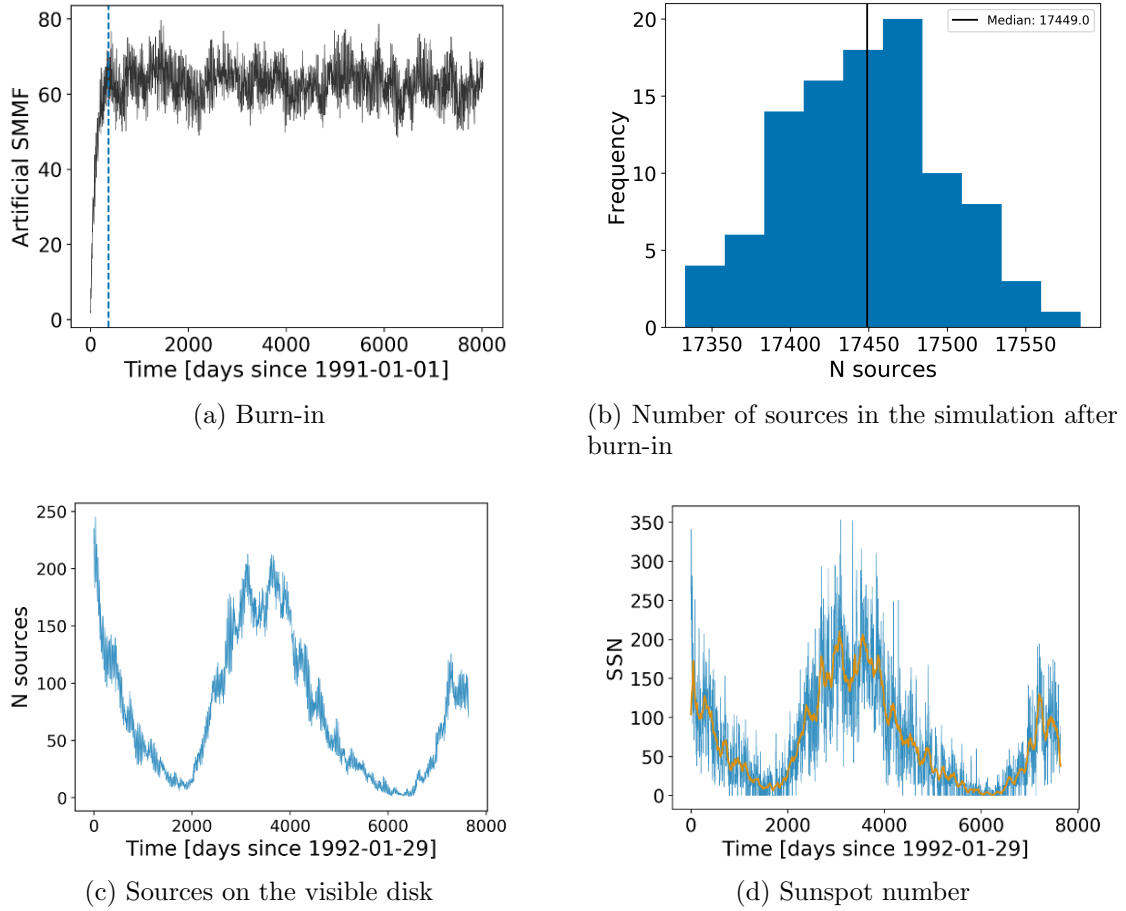


Figure A.4: (a) the burn-in period required to ensure that the interference of sources stabilises. The dashed-vertical line marks one year, showing the sources have stabilised. (b) histogram of the number of sources which remain in the simulation (out of the 20000 input), after the burn-in is removed. (c) the number of simulated sources on the visible disk over the BiSON observational epoch. (d) the daily-averaged sunspot number (blue, and the monthly-averaged sunspot number (orange)).

We included  $\sim 1$ -year for burn-in, such that the interferences between the sources stabilises (see Figure A.4a). After a year the number of sources on the visible disk have steadied, providing a stable SMMF, hence a burn-in period from 01/01/1991



– 29/01/1992 is sufficient. With this burn-in period, we chose to select  $N = 20000$  and  $\tau = 100$  days, which produces a median total of  $\sim 17450$  sources over the BiSON observational epoch of 7633 days, with an average of around 150 – 200 sources per day on the visible disk during solar cycle 23 maximum, as shown in Figure A.4.

### A.3 Outputs

The simulation produces a time series output from the combination of all the sources with and without the inclusion of BiSON observational gaps, along with the Fourier transforms of both.

For quality assurance, a butterfly diagram is also generated per simulation to understand whether the simulation is representative of the Sun’s ARs. A butterfly diagram, from a realisation which allows for a more realistic, stochastic simulation whereby the values for parameters are drawn from a distribution with scatter, is shown in Figure A.5. This butterfly diagram shows a strong resemblance to a true, observational butterfly diagram of the Sun. This provides us with confidence that the simulations are well-representing ARs on the solar disk.

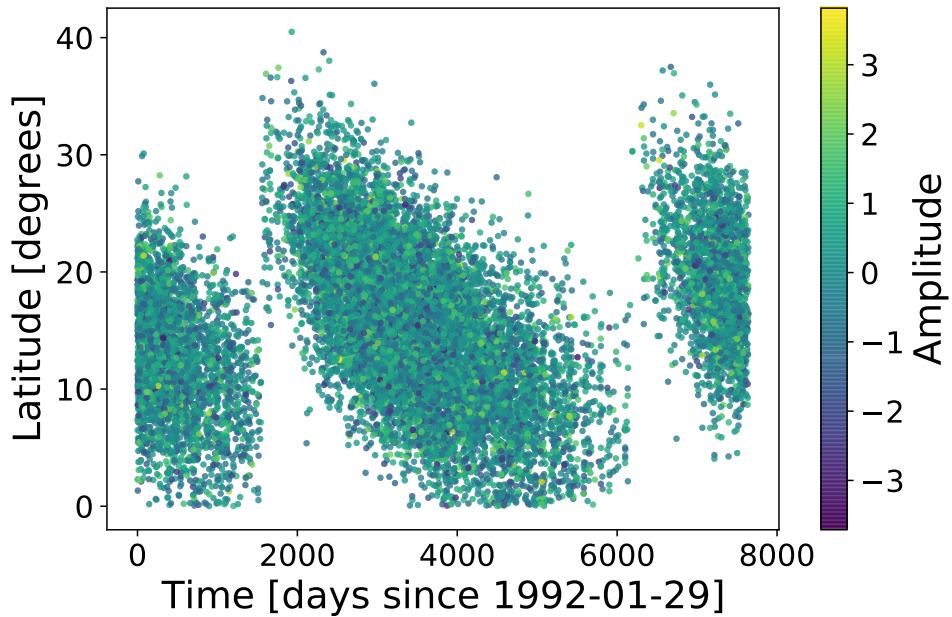


Figure A.5: Artificial butterfly diagram generated from the simulations, allowing for the parameters to be drawn from distributions, to add stochasticity into the simulation.

The resultant power spectra for the two different models (‘cosine’ and ‘sign change’) show different features, which can be seen in the limit spectra shown in Figure A.6. These limit spectra were made by combining 100 realisations of the power spectrum. Each individual power spectrum was made using only a single source starting at  $t_0 = 0$ , and allowing only the phase to vary between the different realisations.

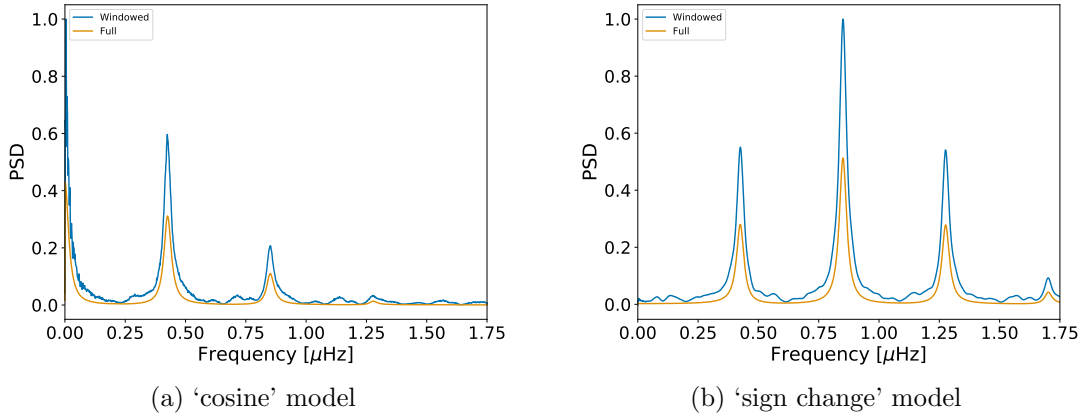


Figure A.6: Limit spectrum from 100 realisations of the cosine model (a) and the sign change model (b) using a single source in each model.

It is clear that the ‘cosine’ model produces a strong peak at the rotational period in the simulation, and a harmonic peak at twice that frequency. This model also produces a significant amount of power at low frequency due to the non-zero mean of the simulated time series.

On the other hand, the ‘sign change’ model has near-zero low frequency power due to the  $\sim$ zero mean of the time series. The ‘sign change’ model also produces a strong peak at half the period of rotation in the simulation. There is a smaller, yet strong peak at the rotational period and at a harmonic of the rotation of 3 times the period. In addition to the limit spectra, we show in Figure A.7 the time series and power spectra for individual realisations of the simulations.

These realisations show the simulated SMMF on a daily cadence. The plots show the stark difference in the time series produced by each model. There are many deviations from a zero mean in the ‘cosine’ model case, which clearly demonstrates

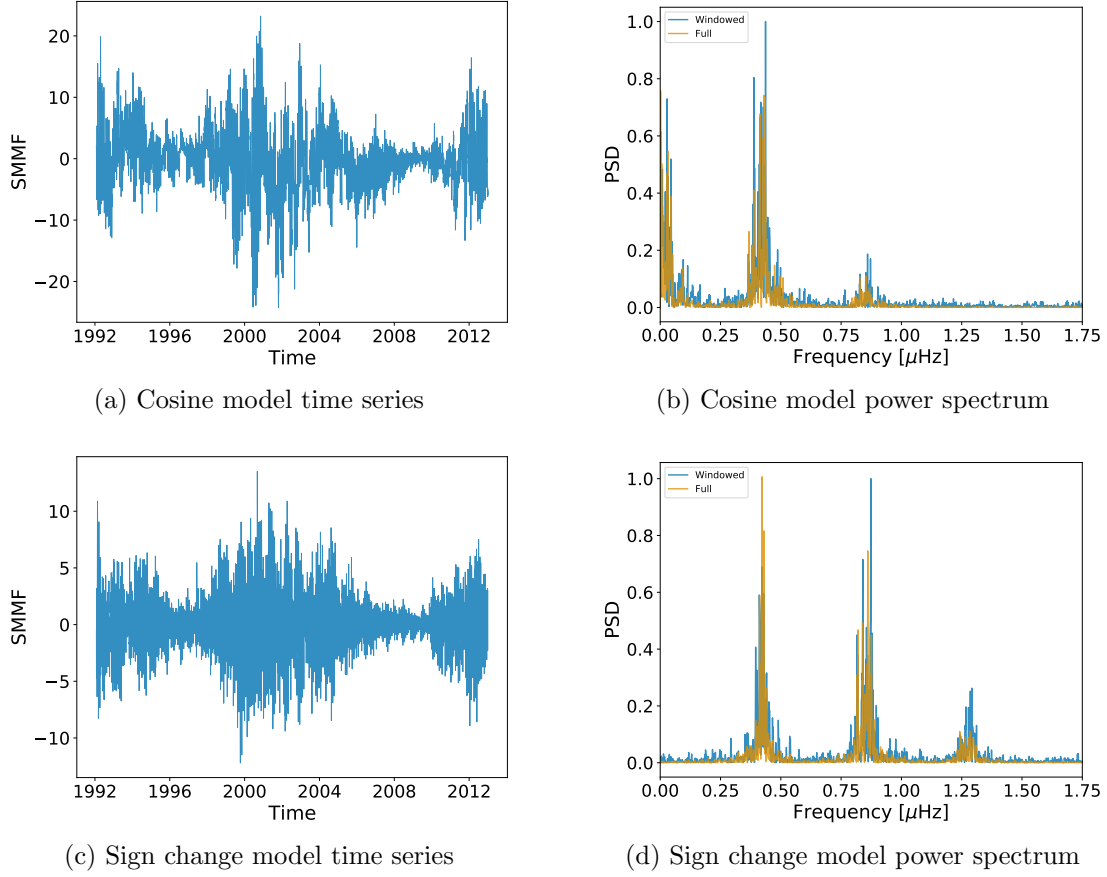


Figure A.7: Time series and power spectra for realisations of the simulations using the cosine and sign change models.

the origin of the low frequency power. In the ‘sign change’ model realisation, the data show a compelling near-zero mean, hence the origin of the near-zero low frequency power in the spectrum.

Both realisations of the simulations result in a time series which does resemble some of the features of the BiSON SMMF observations, and hence there is a justification for using both in combination to simulate a representative model of the SMMF. This is supported also by the power spectra for each realisation, and the limit spectra. The power spectrum of the BiSON SMMF shows a strong harmonic peak at three times the period, which is more prominent in the ‘sign change’ model than the ‘cosine’. The ‘sign change’ model power spectrum also shows a similar splitting around the half-period frequency, resembling that of the BiSON spectrum in Figure 1.4b.

# Bibliography

- Barnes a. W. T., et al., 2020, ApJ, 890, 68
- Basu S., Chaplin W. J., 2017, Asteroseismic Data Analysis: Foundations and Techniques
- Beck J. G., 2000, Solar Physics, 191, 47
- Bose S., Nagaraju K., 2018, The Astrophysical Journal, 862, 35
- Brookes J. R., Isaak G. R., Raay H. B. v. d., 1976, Nature, 259, 92
- Brookes J. R., Isaak G. R., van der Raay H. B., 1978, Mon Not R Astron Soc, 185, 1
- Brown T. M., Christensen-Dalsgaard J., Dziembowski W. A., Goode P., Gough D. O., Morrow C. A., 1989, The Astrophysical Journal, 343, 526
- Chaplin W. J., Appourchaux T., 1999, Mon Not R Astron Soc, 309, 761
- Chaplin W. J., et al., 1996, Solar Physics, 168, 1
- Chaplin W. J., Dumbill A. M., Elsworth Y., Isaak G. R., McLeod C. P., Miller B. A., New R., Pintr B., 2003, Mon Not R Astron Soc, 343, 813
- Chaplin W. J., Elsworth Y., Isaak G. R., Miller B. A., New R., Pintr B., 2005, Mon Not R Astron Soc, 359, 607
- Chaplin W. J., Elsworth Y., New R., Toutain T., 2008, Monthly Notices of the Royal Astronomical Society, 384, 1668
- Christensen-Dalsgaard J., et al., 1996, Science, 272, 1286
- Dacie S., Dmoulin P., Driel-Gesztelyi L. v., Long D. M., Baker D., Janvier M., Yardley S. L., Prez-Surez D., 2016, A&A, 596, A69
- Davies G. R., Broomhall A. M., Chaplin W. J., Elsworth Y., Hale S. J., 2014a, Monthly Notices of the Royal Astronomical Society, 439, 2025
- Davies G. R., Chaplin W. J., Elsworth Y., Hale S. J., 2014b, Mon Not R Astron Soc, 441, 3009
- Dumbill A. M., 1999, PhD thesis, School of Physics and Space Research, University of Birmingham
- Duvall Jr. T. L., Jefferies S. M., Harvey J. W., Osaki Y., Pomerantz M. A., 1993, The Astrophysical Journal, 410, 829

- Elsworth Y., Howe R., Isaak G. R., McLeod C. P., Miller B. A., van der Raay H. B., Wheeler S. J., New R., 1995a. p. 392, <http://adsabs.harvard.edu/abs/1995ASPC...76..392E>
- Elsworth Y., Howe R., Isaak G. R., McLeod C. P., Miller B. A., New R., Wheeler S. J., 1995b, *Astronomy and Astrophysics Supplement Series*, 113, 379
- Foreman-Mackey D., Hogg D. W., Lang D., Goodman J., 2013, *Publications of the Astronomical Society of the Pacific*, 125, 306
- Garca R. A., et al., 1999, *Astronomy and Astrophysics*, 346, 626
- Hale S. J., Howe R., Chaplin W. J., Davies G. R., Elsworth Y., 2016, *Solar Physics*, 291, 1
- Hanasoge S., Mandal K., 2019, *The Astrophysical Journal Letters*, 871, L32
- Handberg R., Campante T. L., 2011, *Astronomy & Astrophysics*, 527, A56
- Harvey K. L., Zwaan C., 1993, *Solar Physics*, 148, 85
- Hathaway D. H., Choudhary D. P., 2008, *Sol Phys*, 250, 269
- Hathaway D. H., Upton L. A., 2020, arXiv e-prints, 2006, arXiv:2006.06084
- Howard R. F., 2001, in , *The Encyclopedia of Astronomy and Astrophysics*. IOP Publishing Ltd, doi:10.1888/0333750888/2297, <http://eaa.crcpress.com/0333750888/2297>
- Howe R., 2009, *Living Reviews in Solar Physics*, 6
- Howe R., Davies G. R., Chaplin W. J., Elsworth Y. P., Hale S. J., 2015, *Mon Not R Astron Soc*, 454, 4120
- Howe R., et al., 2020, *Mon Not R Astron Soc Lett*, 493, L49
- Kotov V. A., 2008, *Astron. Rep.*, 52, 419
- Kotov V. A., 2012, *Bull.Crim. Astrophys. Observ.*, 108, 20
- Kutsenko A. S., Abramenko V. I., Yurchyshyn V. B., 2017, *Sol Phys*, 292, 121
- Lanza A. F., Gizon L., Zaqarashvili T. V., Liang Z.-C., Rodenbeck K., 2019, *A&A*, 623, A50
- Li K. J., Yun H. S., Gu X. M., 2001a, *AJ*, 122, 2115
- Li K. J., Yun H. S., Gu X. M., 2001b, *AJ*, 122, 2115
- Liang Z.-C., Gizon L., Birch A. C., Duvall T. L., 2019, *A&A*, 626, A3
- Löptien B., Gizon L., Birch A. C., Schou J., Proxauf B., Duvall T. L., Bogart R. S., Christensen U. R., 2018, *Nature Astronomy*, 2, 568
- Lund M. N., Chaplin W. J., Hale S. J., Davies G. R., Elsworth Y. P., Howe R., 2017, *Mon Not R Astron Soc*, 472, 3256

- Maunder E. W., 1904, Mon Not R Astron Soc, 64, 747
- McIntosh S. W., et al., 2014, ApJ, 792, 12
- Plachinda S., Pankov N., Baklanova D., 2011, Astronomische Nachrichten, 332, 918
- Rossby C.-G., Collaborators 1939, J Mar Res, 2, 38
- Salvatier J., Wiecki T. V., Fonnesbeck C., 2016, PeerJ Comput. Sci., 2, e55
- Scherrer P. H., Wilcox J. M., Howard R., 1972, Sol Phys, 22, 418
- Scherrer P. H., Wilcox J. M., Kotov V., Severnyj A. B., Severny A. B., Howard R., 1977a, Solar Physics, 52, 3
- Scherrer P. H., Wilcox J. M., Svalgaard L., Duvall Jr. T. L., Dittmer P. H., Gustafson E. K., 1977b, Solar Physics, 54, 353
- Schrijver C. J., Harvey K. L., 1994, Solar Physics, 150, 1
- Severny A. B., 1971, Quarterly Journal of the Royal Astronomical Society, 12, 363
- Snodgrass H. B., 1983, The Astrophysical Journal, 270, 288
- Strohmayer T., Mahmoodifar S., 2014, A Neutron Star Oscillation Mode During a Superburst, <https://slideplayer.com/slide/10313230/>
- Svalgaard L., Wilcox J. M., Scherrer P. H., Howard R., 1975, Sol Phys, 45, 83
- Thomas A. E. L., et al., 2019, Mon Not R Astron Soc, 485, 3857
- Wu C. J., Usoskin I. G., Krivova N., Kovaltsov G. A., Baroni M., Bard E., Solanki S. K., 2018, A&A, 615, A93
- Xiang N. B., Qu Z. N., 2016, AJ, 151, 76
- Xie J. L., Shi X. J., Xu J. C., 2017, The Astronomical Journal, 153, 171
- Zwaan C., 1981, NASA Special Publication, 450
- van Driel-Gesztelyi L., Green L. M., 2015, Living Rev. Sol. Phys., 12, 1